Inferences and Observations of Turbulent Dissipation and Mixing in the Upper Ocean at the Hawaiian Ridge

Joseph P. Martin, Daniel L. Rudnick

Scripps Institution of Oceanography, La Jolla, California, USA

Submitted to the *Journal of Physical Oceanography*

March 10, 2005

Corresponding author address:

Martin, Joseph

Applied Physics Laboratory, University of Washington

1013 NE 40th St., Seattle, WA 98105-6698

Tel: (206) 897-1623 , Fax: (206) 543-6785

e-mail: martin@apl.washington.edu

ABSTRACT

The Hawaiian Ridge is one of the most energetic generators of internal tides in the pelagic ocean. The density and current structure of the upper ocean at the Hawaiian Ridge was observed using SeaSoar and Doppler sonar during a survey extending from Oahu to Brooks Banks and up to 200 km from the ridge peak. The survey observations are used to quantify spatial changes in internal-tide induced turbulent dissipation and mixing. At the Kauai Channel (KC) and French Frigate Shoals / Brooks Banks (FFS/BB) sites, the turbulent dissipation rate of kinetic energy ε and diapycnal eddy diffusivity K_ρ, inferred from established parameterizations, are observed to decay away from the ridge with maxima exceeding minima by 5 times. At both sites, average K_ρ is everywhere greater than the canonical open-ocean value of 10^{-5} m^2 s^{-1}. ε and K_ρ vary along the ridge by up to 100 times and are largest at sites of largest numerical-model internal-tide energy density. In the eastern KC, $K_\rho > 10^{-3}$ m^2 s^{-1} is typical in a patch more than 200 m thick located above the path of an M_2 internal tide ray evident in kinetic energy density. An upper limit on the total dissipation rate within the 4000-m isobath of the Hawaiian Ridge is roughly estimated to be 4.5 GW. Potential density inversions are found near the main ridge axis at significant topographic features. Average K_ρ is larger inside inversions.

1. **Introduction**

Turbulent diapycnal mixing is a necessary component of the meridional overturning circulation of heat and salt (Munk and Wunsch 1998; Wunsch and Ferrari 2004). In mid-latitudes far from convection sites, and at mid-depths beneath the wind-mixed layer and subduction zones and above the bottom boundary layer, diapycnal mixing is the dominant mechanism for transporting heat vertically through the water column. K_ρ, the diapycnal eddy diffusivity, is geographically nonuniform in the pelagic ocean. Observations of a tracer introduced at 300 m depth in the open-ocean mid-latitude Atlantic give a direct estimate of K_ρ of $1.1 \pm 0.2 \times 10^{-5}$ m^2 s^{-1} (Ledwell *et al.* 1993). Velocity microstructure measurements from the same site as the tracer release also indicate a K_ρ of order 10^{-5} m^2 s^{-1} in the upper ocean (Toole *et al.* 1994). Other mid-latitude open-ocean velocity microstructure measurements indicate that K_ρ is no larger than 5×10^{-5} m^2 s^{-1} in the upper 1000 m (Gregg *et al.* 2003). In contrast, at significant topographic features such as ridges and seamounts, upper-ocean K_ρ is ten or more times larger. Within 10 km of the Cobb Seamount in the NE Pacific K_ρ is estimated to be between 10^{-3} and 10^{-1} m^2 s^{-1} at 300 m depth using microstructure measurements (Lueck and Mudge 1997). K_ρ is 10^{-3} m^2 s^{-1} up to 300 m above the Fieberling Seamount which rises to a plain at 600 m depth in the NE Pacific (Kunze and Toole 1997). Inverse models of the mean mid-latitude vertical density structure (Munk and Wunsch 1998) and property budgets for bounded regions (see Table 1. in Wunsch and Ferrari (2004)) require $K_\rho \geq 10^{-4}$ m^2 s^{-1}. The outstanding and oft-posed question then is whether or not enhanced mixing at small areas of significant topography is enough to eliminate the discrepancy between predicted and observed K_ρ in the open ocean. The appropriateness of this question has been challenged because estimates of K_ρ made from observations taken over a month or less leave out processes such as mesoscale eddies which contribute to the predicted K_ρ (Davis 1994a). Regardless, diapycnal mixing is larger at significant topographic features than in the open mid-latitude ocean. An improved understanding of how mixing decays between a significant topographic feature and the open ocean has implications for how mixing is included in global models.

One significant topographic feature where enhanced mixing occurs is the Hawaiian Ridge, a chain of ridges and seamounts that extends for thousands of kilometers in the North Pacific. Microstructure measurements taken during the Hawaii Ocean Mixing Experiment (HOME) indicate K_ρ as large as 3×10^{-4} m^2 s^{-1} over the French Frigate Shoals section of the ridge (Rudnick *et al.* 2003). At Hawaii, local dissipation of internal tides generated at the ridge is hypothesized to be the primary energy source for enhanced mixing. A tidal model which assimilates satellite altimeter measurements of sea surface height indicates that $19{+}6{-}1.5$ GW of the barotropic lunar semidiurnal (M_2) tide is lost at the Hawaiian Ridge through conversion to internal tides or direct dissipation (Zaron and Egbert 2005). Observations from HOME and numerical model results indicate that 10±5 GW fluxes away from the ridge at the 4000-m isobath in M_2 internal tides (Rudnick *et al.* 2003; Merrifield and Holloway 2002). The difference between the barotropic tide energy lost and the outgoing internal tide flux is the amount dissipated within the 4000-m isobath, typically within 50 km of the ridge's topographic peak. This difference is highly uncertain and could be anywhere in the range 2.5 to 20 GW. Using a variety of microstructure observations from HOME and a function for the three-dimensional spatial structure of K_ρ, Klymak *et al.* (2005) estimate the total turbulent dissipation rate within 60 km of the Hawaiian Ridge to be 3±1.5 GW.

As part of HOME we conducted a geographically broad survey of the Hawaiian Ridge obtaining SeaSoar CTD (conductivity-temperature-depth) and ship-based

Doppler sonar velocity observations (Fig. 1). We use the observations to quantify and study the spatial structure of internal wave dissipation and mixing in the upper ocean. The goals of the survey were to observe the transition from enhanced mixing near the ridge to open-ocean levels and to learn about variations in mixing along the ridge. The details of the observations are discussed in Sec. 2.

The amount of internal wave energy available for mixing varies greatly around the Hawaiian Ridge. In the upper ocean, internal wave energy density changes by a factor of ten over across-ridge distances of 100 km and mean-square shear changes by a factor of five in the across- and along-ridge directions (Martin *et al.* 2005) (hereafter MRP). The numerical model results of Merrifield and Holloway (2002) (hereafter MH) show that M_2 internal tide energy density is largest at several "hot spots" along the ridge including: French Frigate Shoals / Brooks Banks (FFS/BB), west of Nihoa I., and the eastern Kauai Channel (KC) just west of the island of Oahu (Fig. 1). The numerical model results also show that vertical modes two and higher carrying 4 GW of M_2 internal tide energy flux across the 4000-m isobath are absent 200 km from the ridge. Only within 100 km of the ridge are energetic internal tide ray structures involving higher modes observed (MH; MRP). At another site of strong topography, the Mendocino Escarpment in the NE Pacific, the only location in the upper ocean with enhanced dissipation ($\varepsilon > 10^{-8}$ W kg^{-1}) is at the terminus of an internal tide ray (Althaus *et al.* 2003). The amount of dissipation and mixing is thus expected to vary significantly across and along the Hawaiian Ridge. Recent results from HOME microstructure measurements indicate an across- and along-ridge structure to K_ρ (Klymak *et al.* 2005).

We use our finescale CTD and Doppler sonar measurements with an internal wave breaking model to infer microscale ε, the turbulent dissipation rate of kinetic energy. We then use this ε in the Osborn (1980) result to estimate K_ρ. Parameterizations of ε resulting from internal wave breaking have been confirmed at a number of sites. In a variety of internal wave environments, Gregg *et al.* (2003) and Polzin *et al.* (1995) found good comparison between ε observed using measurements of centimeter-scale shear and the predictions of parameterizations based upon the internal wave interaction and breaking model of Henyey *et al.* (1986). By considering the transfer of energy to smaller scales resulting from internal wave interaction, Henyey *et al.* (1986) developed an expression for ε occurring at the smallest scales in terms of the energy in the internal wave field at larger scales. Gregg *et al.* (2003), Polzin *et al.* (1995), and others estimate this larger-scale internal wave energy from ten-meter-scale shear and strain observations. The value of the parameterizations is in their wide applicability and that they allow ε to be estimated without the use of specialized instrumentation that resolves centimeter scales. Values of ε determined from microstructure measurements taken during the HOME survey are consistent with the Gregg (1989) parameterization to within a factor of two over the range $5{\times}10^{-10}$ to 10^{-7} W kg^{-1} (Lee *et al.* 2005). Lee et al.'s observation supports our use of the Gregg (1989) and Gregg *et al.* (2003) methods in Sec. 3 as tools to investigate the spatial structure of turbulent dissipation and mixing.

A decrease in potential density with increasing depth indicates a gravitationally unstable portion of the water column. This temporary inversion in potential density is the result of recent overturning. Overturning transports heat and salt and thus results in vertical mixing. With SeaSoar CTD data, we use inversions to identify locations of active mixing. Using SeaSoar data Ullman *et al.* (2003) observed 20 m high inversions over the northern edge of Georges Bank. At an energetic coastal site, Alford and Pinkel (2000a) find that temperature and density inversions larger than 2 m occur preferentially at times and depths of lower stratification (higher strain), lower gradient Richardson number, and higher strain rate. In Sec. 4, we map the locations of resolvable potential density inversions and investigate their collocation with enhanced K_ρ estimated in Sec. 3.

2. Data

The SeaSoar / Doppler sonar survey was made between 29 August and 29 September 2000 (Fig. 1). Two along-ridge surveys followed approximately the 1000-m isobath between the island of Oahu and the shallow banks located just west of FFS at about (24°N, 167°W). Across-ridge surveys were made at FFS/BB and at KC. Motivated by the observation of large isopycnal displacements, one leg of the survey at KC was repeated eight times. An across-ridge survey west of the island of Kauai and a combined along/across-ridge survey were also made. SeaSoar was flown in a vertical sawtooth pattern between about 20 and 370 m depth at a tow speed of 4.1 m s^{-1}. The SeaSoar / Doppler sonar data processing is discussed in MRP. Density inversions are investigated using the SeaSoar CTD data averaged to one-second intervals. The estimates of ε from the parameterizations are made using the CTD and 50 kHz Doppler sonar data grid-averaged to 15 minute time intervals and 6.15 m depth intervals. Details of the Sea Soar / Doppler sonar processing relevant to the analysis in Secs. 3-4 are included in those sections.

3. Estimates of the Dissipation Rate and the Diapycnal Eddy Diffusivity from Parameterizations

The turbulent dissipation rate of kinetic energy is estimated from the SeaSoar / Doppler sonar data using two methods. The first estimate, $\varepsilon_{\mathrm{IW1}}$, is obtained at each point in the CTD / Doppler sonar grid using the method of Gregg (1989). The second estimate, $\varepsilon_{\mathrm{IW2}}$, providing an average value over the upper ocean and over some horizontal region, is obtained using a method described by Gregg *et al.* (2003). The procedure used to compute $\varepsilon_{\mathrm{IW1}}$ and $\varepsilon_{\mathrm{IW2}}$ is in the appendix. K_ρ is computed from the $\varepsilon_{\mathrm{IW1}}$ and $\varepsilon_{\mathrm{IW2}}$ estimates using $K_\rho = 0.2\varepsilon/N^2$ where N is the buoyancy frequency, the result of a balance in turbulent kinetic energy among turbulent production, work against buoyancy, and dissipation (Osborn 1980).

K_ρ is frequently observed to be larger than 10^{-5} m^2 s^{-1}. Particulary large values of K_ρ are observed during a crossing of the Kauai Channel at the peak of spring tide (M_2 and S_2 barotropic tidal constituents in phase) (Fig. 2a). These large values are potentially the result of internal tide dissipation. MRP observed a region of enhanced internal-wave kinetic energy density along an across-ridge path extending from the northern edge of the ridge peak in the eastern Kauai Channel to a point at the surface on the south side of the ridge. This path is consistent with an M_2 internal tide ray, the path along which M_2 internal tide energy propagates. In Fig. 2a, K_ρ is largest above where this ray intersects the section (designated by the pink circle). (The size of the circle is chosen purely for visualization and is not related to any hypothesis about ray dimensions.) Values of K_ρ in excess of 10^{-3} m^2 s^{-1} are typical for over 200 m above the ray. K_ρ values of 10^{-2} m^2 s^{-1} are not uncommon. Much lower K_ρ is observed during a second crossing made at the end of the neap half of the spring-neap cycle (Fig. 2b). Fig. 2a demonstrates strong mixing, as predicted by the K_ρ estimate, occurs near the Hawaiian Ridge. The observation of this strong mixing near the ray and at the peak of spring tide, suggests the mixing results from the dissipation of semidiurnal internal tides. In Secs. 3a-b we investigate the across- and along-ridge spatial structure of the enhanced dissipation and mixing present near the Hawaiian Ridge. In Sec. 3c an attempt is made to integrate ε over the entire ridge to obtain a total value of the dissipation rate.

a. Across-Ridge Structure

In this section, data from the across-ridge surveys at the KC and FFS/BB sites are used to investigate the spatial structure of averaged $\varepsilon_{\mathrm{IW1}}$ and $\varepsilon_{\mathrm{IW2}}$ and corresponding averaged K_ρ. Two averages are used. The first average, designated by $\{\}$, is a horizontal mean over all profiles that fall within bins 10 km wide in position normal to the ridge. The second average, designated by $\langle\rangle_{\mathrm{d}}$, is a vertical mean over the depth range 100 m (well below the mixed layer base) to 550 m (the range of the Doppler sonar). The results of this averaging are shown in Fig. 3 for KC and Fig. 4 for FFS/BB. The mean-square shear magnitude $\langle\{S^2\}\rangle_{\mathrm{d}}$ is shown in panel (a) of each figure. The shear magnitude is computed from first-differences:

$$S^2 = \left[(\Delta u/\Delta z)^2 + (\Delta v/\Delta z)^2\right] \qquad [\mathrm{s}^{-2}]. \tag{1}$$

The difference interval Δz is the vertical grid spacing of 6.15 m and u and v are, respectively, the east and north components of velocity from the Doppler sonar. Note that the $\{\}$ and $\langle\rangle_{\mathrm{d}}$ means are built into the definitions of $\varepsilon_{\mathrm{IW2}}$ and $K_\rho(\varepsilon_{\mathrm{IW2}})$ (see appendix). There is good agreement between $\varepsilon_{\mathrm{IW1}}$ and $\varepsilon_{\mathrm{IW2}}$ and between $K_\rho(\varepsilon_{\mathrm{IW1}})$ and $K_\rho(\varepsilon_{\mathrm{IW2}})$ at both the KC and FFS/BB sites (Figs. 3 and 4). On the south side of the ridge at KC there are a few positions where the two estimates differ by a factor of up to 3. The agreement is better at FFS/BB. Thus, our values for the turbulent dissipation rate are not very sensitive to whether the IW1 or IW2 method is used. Below, general mention of ε and K_ρ refers to both the IW1 and IW2 estimates.

Across-ridge trends in $\langle\{\varepsilon\}\rangle_{\mathrm{d}}$ and $\langle\{K_\rho\}\rangle_{\mathrm{d}}$ are present on both sides of the ridge at KC and on the south side at FFS/BB (Figs. 3b-c and 4b-c). The trends show maximum values of $\langle\{\varepsilon\}\rangle_{\mathrm{d}}$ and $\langle\{K_\rho\}\rangle_{\mathrm{d}}$ exceeding minimum values by five or more times. At all displayed across-ridge positions at both sites $\langle\{K_\rho\}\rangle_{\mathrm{d}}$ exceeds the canonical observed open-ocean value of 10^{-5} m^2 s^{-1}. At KC, $\langle\{\varepsilon\}\rangle_{\mathrm{d}}$ and $\langle\{K_\rho\}\rangle_{\mathrm{d}}$ are maximum between positions -25 and 5 km. At FFS/BB, we did not repeatedly survey within

15 km of the ridge peak because of the shallow topography, and cannot determine how large average mixing is there. Far from the ridge on the north side $\langle\{\varepsilon\}\rangle_{\mathrm{d}}$ and $\langle\{K_\rho\}\rangle_{\mathrm{d}}$ are larger at FFS/BB. On the south side $\langle\{\varepsilon\}\rangle_{\mathrm{d}}$ and $\langle\{K_\rho\}\rangle_{\mathrm{d}}$ have larger maxima at FFS/BB than at KC. Large $\{K_\rho\}$ is often observed below 300 m, and $\{K_\rho\}$ outside of maxima is typically larger at FFS/BB (Figs. 3d and 4d).

Across-ridge gradients of ε and K_ρ are important quantities for understanding the length scales separating locations of enhanced mixing such as Hawaii from the open ocean. We estimate the across-ridge gradients $d(\log_{10}(\varepsilon))/dx$ and $d(\log_{10}(K_\rho))/dx$ at KC and on the south side of FFS/BB by using exponential fits to ε and K_ρ. For example with $K_\rho = K_\rho^{max} e^{a(x-x_0)}$, $d(\log_{10}(K_\rho))/dx = a \log_{10} e$. The variable x is the across-ridge position relative to the ridge peak. At KC one exponential curve is fit from position -170 km to the position x_0 of the maximum in the IW1 or IW2 estimate and the second curve from the maximum to position 170 km. At FFS/BB an exponential curve is fit from position -120 km to the maximum. The fits are shown as the dashed lines in Figs. 3 and 4. The resulting across-ridge gradients per 100 km are listed in Table 1. At KC, these gradients correspond to a factor of 2.4 to 3.9 change in ε and K_ρ over 100 km on the south side of the maximum depending on whether the IW1 or IW2 method is used. There is roughly a factor of 0.5 change over 100 km on the north side. On the south side of FFS/BB there is a factor of 3.3 to 4.8 change in ε and K_ρ over 100 km depending on whether IW1 or IW2 is used. Another way to think about the gradients is in terms of the e-folding length scales of the fits $(1/|a|)$ and these are listed in Table 1 as well. Klymak *et al.* (2005) report on the across-ridge structure of K_ρ at the Kauai Channel using direct measurements of ε from an instrument towed at 700 m and deeper. We can compare our $d(\log_{10}(K_\rho))/dx$ values with a value for KC extracted from Fig. 8 in Klymak *et al.* (2005). Beyond 5 km south of the ridge peak Klymak *et al.* (2005) have $d(\log_{10}(K_\rho))/dx$ of approximately

2 per 100 km, 3.4 times larger than the IW1 estimate in Table 1 and 4.8 times larger than the IW2 estimate. They report an even larger gradient closer to the ridge peak. One explanation for the discrepancy is that the across-ridge gradient of K_ρ is strongly depth-dependent, differing greatly between the upper-ocean region from beneath the mixed layer to 550 m and the region 700 m and deeper. Another explanation for the discrepancy is the differences in the averaging methods used.

b. Along-Ridge Structure

The change in ε and K_ρ with geographic location can be studied using maps (Figs. 5 and 6). The quantities displayed in the maps are $\log_{10}(\langle\varepsilon_{\mathrm{IW1}}\rangle_b)$ and $\log_{10}(\langle K_\rho(\varepsilon_{\mathrm{IW1}})\rangle_b)$ where $\langle\rangle_b$ is a mean over all profiles that fall within regularly-spaced 20 km × 20 km boxes and over the depth range 100-550 m. The middle values of the colorbars in Figs. 5 and 6 are near the modes of the PDFs of $\log_{10}(\langle\varepsilon_{\mathrm{IW1}}\rangle_b)$ and $\log_{10}(\langle K_\rho(\varepsilon_{\mathrm{IW1}})\rangle_b)$. For both figures, more than 95% of the values fall within the colorbar ranges. The geographic distribution of $\varepsilon_{\mathrm{IW1}}$ and $K_\rho(\varepsilon_{\mathrm{IW1}})$ is non-uniform. The observed locations of largest dissipation and mixing can be compared with the predicted locations of largest M_2 internal tide generation along the Hawaiian Ridge. Specifically our comparison is with Figs. 3-5 in MH. The collocation of largest baroclinic energy density and energy flux density from MH with largest $\log_{10}(\langle\varepsilon_{\mathrm{IW1}}\rangle_b)$ and $\log_{10}(\langle K_\rho(\varepsilon_{\mathrm{IW1}})\rangle_b)$ is indicative of localized dissipation of M_2 internal tides. There is collocation at FFS/BB, west of Nihoa I. centered at about 163°W, and in the eastern KC. Over the section of ridge observed in the survey, FFS/BB appears to be the site of overall largest generation and dissipation. There is also collocation between quieter regions such as from 165-164.5°W and from 162.5-161.5°W. There are differences, however. For example, there is enhanced dissipation and mixing at the seamount at 161°W and south of Kauai, both places in MH without strong internal tide generation. Changing the size of the boxes to have side 10 km or 40 km does not alter conclusions about what locations have the most dissipation and mixing.

c. Integrated Dissipation

The integral of the turbulent dissipation rate over the Hawaiian Ridge is an important quantity because it is an upper limit on the total loss rate of internal tide energy near the ridge and thus an upper limit on the rate at which energy is available for mixing. The integral can be considered an upper limit because internal tide dissipation is likely not the only source of nonzero ε near the ridge. Ideally, the value of the energy loss rate for internal tides generated at the ridge would be determined by integrating long-time mean ε

-from the ocean surface to the bottom,

-along all sections of the ridge that are significant internal tide generators,

-and across-ridge from the ridge peak to the position beyond which internal tides persist as stable low modes.

The ideal integral is of course not possible given the limits on our survey observations, but a reasonable upper limit on the total dissipation rate is obtainable. The best estimates of the mean spatial structure of ε are at KC and FFS/BB, sites where ε is typically larger than elsewhere along the ridge. We apply the mean across-ridge structure of ε at KC and FFS/BB to the entire ridge to obtain upper limits on the total dissipation rate. This procedure potentially under-utilizes data taken at other locations. At various locations along the ridge, including some more than 50 km from the ridge peak (Fig. 5), large ε is observed during one-time ship passes. However, the mean ε at these locations is unknown, and for that reason these values are not used in computing the integral.

The first step in the integration is to obtain the depth integral of $\{\rho\}\{\varepsilon\}$ at each across-ridge position shown in Figs. 3 and 4. The variable ρ is density. For $\varepsilon_{\mathrm{IW1}}$, the depth integral over the vertical coordinate z is defined by:

$$\int_{-d_B}^{-d_T} \{\rho\}\{\varepsilon_{\mathrm{IW1}}\}dz \tag{2}$$

The limits are $d_T = 100$ m and $d_B = 550$ m. Significant dissipation of internal tides could occur shallower than 100 m, but the parameterizations do not apply to the mixed layer. For $\varepsilon_{\mathrm{IW2}}$, the depth integral is given by $(\langle\{\rho\}\rangle_d\langle\{\varepsilon_{\mathrm{IW2}}\}\rangle_d)(d_B - d_T)$. The depth range integrated over is limited to the upper ocean, but a substantial fraction of the dissipation is expected to occur there. At the 3000-m isobath of the Hawaiian Ridge, depths below 1000 m typically only contribute 12% to the full-depth integral of the turbulent dissipation rate (Lee *et al.* 2005). The cumulative integral over across-ridge position x is computed by integrating from over the ridge outwards to each south side x and by integrating from over the ridge outwards to each north side x (Fig. 7). Simplistic estimates of the total dissipation rate D within a distance d of the ridge are obtained by adding the Fig. 7 values at positions -d and d and by multiplying the result by a ridge length of 2500 km. The ridge length of 2500 km is the length over which most of the barotropic tidal loss and internal tide generation occurs (Egbert and Ray 2000; Merrifield and Holloway 2002). As discussed in the Introduction, about 10 GW of M_2 internal tide energy is predicted to be available for dissipation within the 4000-m isobath, although with much uncertainty. At KC and FFS/BB the 4000-m isobath is roughly 50 km from the ridge peak. Integration out to 50 km using the across-ridge structure at KC gives $D(\varepsilon_{\mathrm{IW1}}) = 2.5$ GW and $D(\varepsilon_{\mathrm{IW2}}) = 1.4$ GW. Using FFS/BB's across-ridge structure, integration to 50 km gives $D(\varepsilon_{\mathrm{IW1}}) = 2.5$ GW and $D(\varepsilon_{\mathrm{IW2}}) = 2.3$ GW. At both sites, $D(\varepsilon_{\mathrm{IW1}}) > D(\varepsilon_{\mathrm{IW2}})$. The integrals can be extended to the ocean floor by accounting for the fraction of total dissipation occurring beneath 550 m. The fraction is determined using $K_\rho = 0.2\varepsilon/N^2$

and Klymak et al.'s (2005) vertical structure function for K_ρ:

$$Z(h/H) = \begin{cases} 1 & h/H > 0.55 \\ 10^{1.18(1-\frac{h}{0.55H})} & h/H < 0.55 \end{cases} \tag{3}$$

where h is the height above the bottom and H is the ocean depth. N for the extension is from an exponential fit to the average of three full-depth Hawaii Ocean Time Series (HOTS) profiles taken north of the Kauai Channel near the time of the survey. The resulting full-depth (fd) dissipation rates are $D_{\mathrm{fd}}(\varepsilon_{\mathrm{IW1}}) = 4.4$ GW and $D_{\mathrm{fd}}(\varepsilon_{\mathrm{IW2}}) = 2.5$ GW using KC's across-ridge structure and $D_{\mathrm{fd}}(\varepsilon_{\mathrm{IW1}}) = 4.3$ GW and $D_{\mathrm{fd}}(\varepsilon_{\mathrm{IW2}}) = 3.9$ GW using FFS/BB's structure. The across-ridge integral at FFS/BB begins 20 km from the ridge peak, so substantial dissipation may be unaccounted for there. In summary, the upper limit on the total dissipation rate of turbulent kinetic energy within the 4000-m isobath of the Hawaiian Ridge is about 4.5 GW. This compares favorably with the upper end of the range 3±1.5 GW obtained by Klymak *et al.* (2005), also for a 2500-km long Hawaiian Ridge, but across-ridge to 60 km from the ridge peak.

4. Observations of Mixing Using Potential Density Inversions

a. Methods

Many instances of decreasing potential density σ_θ with increasing depth occur in the 1-second SeaSoar records. A procedure is required to retain true inversions from among these instances and reject spurious ones. Our procedure mainly follows that of Ullman *et al.* (2003) and Galbraith and Kelley (1996). The first step is to isolate pieces of the SeaSoar sawtooth record with monotonic increases or decreases in depth of 300 or more meters (down profiles and up profiles, respectively). Each observed profile of σ_θ is then sorted to obtain the stable profile $\hat{\sigma_\theta}$ with the property that $\hat{\sigma_\theta}$ always increases with depth. If the value $\sigma_\theta(z_i)$ at depth z_i is assigned to depth z_j in the sorted profile, its Thorpe displacement is $d' = z_j - z_i$. Inversions are defined by points with $d' \neq 0$ between two points with $d' = 0$. Inversions are checked for the property that the sum of d' within each inversion equals zero. Concatenation of neighboring inversions is sometimes required to achieve this property. Once inversions are identified a number of quantities for each inversion are computed. The Thorpe scale L_T is the root-mean-square (rms) Thorpe displacement:

$$L_\mathrm{T} = \overline{(d'^2)}^{1/2} \tag{4}$$

where the overbar implies a mean over all points in each inversion. The inversion height is denoted L_Z. The range of potential density in each inversion is denoted $(\sigma_\theta)_\mathrm{Z}$. The buoyancy frequency assigned to each inversion is $\overline{N}$ where N is computed using $\hat{\sigma_\theta}$. The values $\overline{\Delta z}$ and $\overline{w}$ are, respectively, the mean depth spacing between successive points and mean SeaSoar vertical speed in each inversion.

Several steps are then used to separate true inversions from spurious ones. As discussed by Ullman *et al.* (2003), if the slope of the SeaSoar trajectory is less than the slope of an internal wave SeaSoar is passing through, a spurious inversion can result. Internal waves in the presence of no ambient shear become unstable with waveheight to wavelength ratio of greater than 0.1 (Thorpe 1978). A maximum rms internal wave slope in the upper ocean at Hawaii of 0.003 was observed by MRP. To be cautious we only accept inversions with mean SeaSoar trajectory slope greater than 0.1. This is accomplished by requiring $\overline{w} > 0.4$ m s^{-1} which follows from a tow speed of 4 m s^{-1}. The tow speed only varies between 3.9 and 4.3 m s^{-1}. Virtually all inversions centered at depths between 70 and 320 m have $\overline{w} > 0.4$ m s^{-1}. Only inversions with $L_\mathrm{Z} > 2\overline{\Delta z}$ are accepted. The factor of 2 is the minimal Nyquist requirement. A local $\overline{\Delta z}$ for each inversion is used because SeaSoar does not have a constant vertical velocity during profiling and thus the vertical spacing of the 1 second data ranges from 0.25 to 3 m. Accepted inversions are also required to have $(\sigma_\theta)_{\mathrm{Z}}$ greater than the error in σ_θ. SeaSoar is equipped with two pairs of conductivity and temperature sensors, one pair on each of the lower tail wings. The rms difference in σ_θ determined from the two sensor pairs is a measure of error in σ_θ. Below the mixed layer this error is typically 1-3$\times 10^{-3}$ kg m^{-3}. All accepted inversions have $(\sigma_\theta)_{\mathrm{Z}} > 3 \times 10^{-3}$ kg m^{-3}. Of 64,703 inversions initially identified, the slope, L_{Z}, and $(\sigma_\theta)_{\mathrm{Z}}$ requirements leave only 2,301 as accepted inversions. The run-length test outlined by Galbraith and Kelley (1996) is then applied to the remaining inversions. A "run" is a set of consecutive d' values all with the same sign. For each inversion, the maximum run length r, the number of values in the longest run, is recorded. The probability density function (PDF) of r from all inversions is compared to the theoretical PDF of run-length noise for which positive and negative d' are equally likely (The same PDF applies to coin tossing.). For run-lengths greater than or equal to 4, the PDF of r is twice the noise PDF. Inversions with $r \geq 4$ are accepted, leaving 906 inversions. About 20% of these inversions are then rejected using the water-mass test of Galbraith and Kelley (1996) which requires a tight relationship between potential temperature θ and salinity S. After visual inspection of the $\theta - S$ relationship for inversions, we choose water-mass-test criteria less strict than those of Galbraith and Kelley (1996) by a factor of 2. The result of the overall procedure is acceptance of 297 inversions below the mixed layer. Our observations of inversions with a towed profiler are certainly of lower quality than those obtained by vertical profiling. However, turbulent patches in the ocean are horizontally elongated with a typical vertical to horizontal dimension aspect ratio of order 0.01 to 0.1 (Gregg 1987). Because the SeaSoar trajectory slope for retained inversions always exceeds

0.1, inversion evidence of turbulent mixing is within the scope of our observations.

Dillon (1982) found an empirical linear relationship between the Thorpe scale L_{T} and the Ozmidov scale $L_{\mathrm{O}} = (\varepsilon/N^3)^{1/2}$ that can be used to obtain an inversion-based estimate of the dissipation rate:

$$\varepsilon_{\mathrm{T}} = 0.64 L_{\mathrm{T}}^2 \overline{N}^3. \qquad (5)$$

However, this relationship is contingent upon the gradient Richardson number (Ri) being approximately constant, which is not true of our observations. If the Ri dependency is retained, the inversion-based estimate of ε depends much more strongly on Ri than on L_{T} or $\overline{N}$, and cannot be considered independent from the $\varepsilon_{\mathrm{IW1}}$ and $\varepsilon_{\mathrm{IW2}}$ estimates. Thus, we choose not to use Eq. 5, even though it has been regularly used in the literature without consideration of the range of Ri.

b. *Results for Accepted Inversions*

Several of the inversions have fairly large vertical extent. Four inversions in σ_θ with $L_{\mathrm{Z}} > 25$ m are shown in Fig. 8 along with the sorted $\hat{\sigma_\theta}$ profiles. Each of these inversions appears in the full-depth σ_θ profile with $|d\sigma_\theta/dz|$ clearly smaller than values just outside of the inversion. One inversion from west of Nihoa I. in the first along-ridge survey extends over 39.6 m depth and includes several sub-inversions (panel (a)). An inversion south of Nihoa I. in the second along-ridge survey (panel (b)) and another 42 km from the ridge in the Kauai Channel (panel (c)), both have tall Z-shapes. Near Kaula I., a profile of σ_θ exhibits instability over a 45-m depth range (panel (d)). The inversions in Fig. 8 are extreme cases. The distribution of L_{T}, L_{Z}, and $\overline{N}$ for all inversions can be examined by looking at their PDFs (Fig. 9). Log values are used as each property has a roughly lognormal distribution. The L_{T} and L_{Z} PDFs are meaningful for values at the mode or greater. The mode of the L_{T} PDF is 3 m, and the mode of the L_Z PDF is 4 m. The decrease in the PDFs for values less than the mode is a result of the inability to resolve small inversions. In contrast to Fig. 9, one would expect the true PDFs to monotonically increase with decreasing L_T and L_Z. The mode of the $\overline{N}$ PDF is 2×10^{-3} rad s^{-1}. Most of the inversions with $\overline{N} > 4 \times 10^{-3}$ rad s^{-1} are from near the mixed layer base. The deepest inversions we observe with SeaSoar are near 350 m depth. At this depth, typical values of the along-track mean buoyancy frequency used to compute $\varepsilon_{\mathrm{IW1}}$ are greater than 6×10^{-3} rad s^{-1}. This value corresponds to $\log_{10} \overline{N} = -2.2$. Thus, the inversions well beneath the mixed layer base have a local buoyancy frequency less than the deepest (and hence smallest) observed mean values.

The value of our observations is in the ability to examine the spatial distribution of inversions around the ridge to look for a pattern in their occurrence. Also of interest is how the size of the inversions and their fraction of occurrence changes around the ridge. We compute mean L_Z and the fraction of occurrence and display them on maps (Figs. 10 and 11). The mean is over all inversions below 100 m depth that fall within the boxes defined in Sec. 3b. Fraction of occurrence is the sum of L_Z over all inversions in each box divided by the sum of available depth ranges over all profiles in that box. Thus, it is just the mean fraction of the water column that is inverted. Due to the sparse occurrence of accepted inversions, many boxes contain none. Most displayed boxes contain only one inversion, but one box centered at (23.15°N,163.11°W) contains 14 and several near the ridge in the eastern KC contain more than 5. The most apparent result is that accepted inversions occur most frequently near the main ridge axis. This can be seen by comparing the boxes displayed in Figs. 10 and 11 with all available boxes shown in Figs. 5 and 6. The inversions congregate near the ridge at FFS/BB, west of and near Nihoa I., around Kaula I., Niihau I., and Kauai I. between 160.6°W and 159.4°W, and in the eastern

KC. Inversions tend to be absent farther from the ridge. There are virtually none on the northern side of the KC, a region that was well sampled. More are found far from the ridge at FFS/BB and where sampling was heaviest on the south side of KC. Inversions are not found at the gaps in the ridge between 162°W and 160°W, nor at the Necker I. section of ridge centered at 164.5°W. It is difficult to discern clear patterns in the properties shown in Figs. 10 and 11, a result of having such a small number of inversions in any one box. Consistently large mean L_{Z} is found east of FFS and west of Nihoa I.. There is a large fraction of occurrence of inversions west of Nihoa I.

The collocation of inversions with large values of $K_\rho(\varepsilon_{\mathrm{IW1}})$ suggests that energy dissipated by internal waves is used in vertical mixing. To investigate this collocation, a comparison can be made between the pdf of $K_\rho(\varepsilon_{\mathrm{IW1}})$ inside and outside of accepted inversions (Fig. 12). K_ρ is used instead of $\varepsilon_{\mathrm{IW1}}$ to reduce effects of depth dependence since K_ρ has less depth dependence in the upper ocean than ε (Lee *et al.* 2005; Klymak *et al.* 2005). The grid point of each $K_\rho(\varepsilon_{\mathrm{IW1}})$ value is considered inside an inversion if it is the closest point in time to that inversion and if it falls within the depth range of the inversion. Values of order 10^{-4} and 10^{-3} m^2 s^{-1} occur more frequently inside inversions than outside inversions. The inside mean is 2.5×10^{-4} m^2 s^{-1} and the outside mean is 1.5×10^{-4} m^2 s^{-1}, a relative difference of 45%. The inside median is 2.2×10^{-5} m^2 s^{-1} and the outside median is 1.1×10^{-4} m^2 s^{-1}, a relative difference of 68%. The differences in average $K_\rho(\varepsilon_{\mathrm{IW1}})$ inside and outside of inversions suggest that enhanced dissipation of internal wave energy results in apparent mixing.

5. **Summary and Conclusions**

The goal of this study was to quantify turbulent dissipation (ε) and mixing (K_ρ) and investigate their spatial structure in the upper-ocean pycnocline at the Hawaiian

Ridge. This was accomplished with finescale observations of density (meter-scale) and shear (ten-meter-scale) from a survey that covered over 1000 km of the ridge length. These observations were used in two ways: as input into parameterizations of ε based on ten-meter-scale internal wave properties and to look for large density inversions. We were thus able to learn about the spatial structure of internal-wave dissipation and resulting mixing without fully resolving these processes.

The observed across-ridge structure demonstrates that a major part of the transition from enhanced mixing at the Hawaiian Ridge to open-ocean background conditions occurs within the range of our observations. When averaged over 100-550 m depth and over bins 10 km wide in across-ridge position, across-ridge trends in ε and K_ρ are found at the Kauai Channel (KC) and south of French Frigate Shoals / Brooks Banks (FFS/BB) with maxima exceeding minima by 5 or more times. Exponential fits to the across-ridge structure of ε and K_ρ are useful to quantify the trends. The fits indicate $K_\rho(\varepsilon_{\mathrm{IW1}})$ has an e-folding length scale of about 80 km for the south side of KC and FFS/BB and 150 km for the north side of KC (Table 1). Suppose that the parameterizations of ε have a valid dependence on shear and that internal tides generated at Hawaii are a large contributor to this shear. Our results then indicate that where there are large across-ridge trends (south-side KC and FFS/BB), 2.5 to 5 times more internal tide energy is dissipated at the maximum in ε than at an additional 100 km away from the ridge peak. However, far from the ridge there may still be significant mixing. For example, 80 km from the ridge peak, south and west of Nihoa I., there are large values of ε and K_ρ. It is unknown whether these large values occur on average so far from the ridge. The absence of an across-ridge trend in K_ρ north of FFS/BB is possibly due to the focusing of internal tides into this region by the bend in the ridge, concave to the north side (MRP).

Averaged over 100-550 m depth and over regularly spaced boxes with side of 20 km, ε and K_ρ are found to vary along the ridge by up to two orders of magnitude. The largest values of ε and K_ρ tend to be collocated with the largest values of energy density and flux density in the internal tide generation numerical model of Merrifield and Holloway (2002). The sites of collocation are FFS/BB, west of Nihoa I., and the eastern KC. FFS/BB is the site of largest internal tide generation in the MH model and largest dissipation in our observations. Significant dissipation is not apparently limited to the three main sites, however, as large values are also observed southeast of FFS near a smaller ridge, at the seamount at 161°W, and south of Kauai. A conclusion suggested by both the across- and along-ridge spatial structure is that substantial dissipation of the internal tides occurs close to where they are generated.

Temporal changes over the spring-neap cycle are also important. At one location in the eastern KC between 200 and 450 m depth and over the 1000-m isobath, typical values of K_ρ decrease by two or more orders of magnitude between the peak of spring tide and the end of neap tide. This change occurs immediately above the location of an M_2 internal tidal ray of largest kinetic energy density emanating from the ridge (MRP). We can speculate that M_2 internal tides become unstable within or near the ray, dissipating in part at an across-ridge position just south of the ridge peak.

Our results and conclusions concerning the magnitude of dissipation and mixing are less certain than those concerning their spatial structure. We do not test the accuracy and functional dependencies of the ε parameterizations. However, Lee *et al.* (2005) found that values of ε determined from microstructure measurements taken during the HOME survey are consistent with the (Gregg 1989) parameterization (IW1) to within a factor of two over the range 5×10^{-10} to 10^{-7} W kg^{-1}. All values of K_ρ shown in Figs. 3 and 4 computed with the parameterizations are greater than the canonical open-ocean value of 10^{-5} m^2 s^{-1}. Maximum values are greater than 10^{-4} m^2 s^{-1}. In the upper ocean, we have addressed a very basic objective of the

HOME project by learning that K_ρ is enhanced near the Hawaiian Ridge, supporting the results of others (Klymak *et al.* 2005). Integrating out to 50 km from the ridge, near the 4000-m isobath, we obtain an upper bound on the dissipation rate of about 4.5 GW for a 2500 km long ridge. This is in agreement with the upper end of the range 3 ± 1.5 GW obtained by Klymak *et al.* (2005) also for a 2500 km ridge.

Our observations of density inversions provide direct evidence of large mixing events occurring near the Hawaiian Ridge. Extreme cases have vertical dimension of order tens of meters. The spatial distribution of these large mixing events supports the results obtained from the estimates of K_ρ; mixing events are largest near the ridge and at certain locations along the ridge. Resolved inversions occur mostly near the main ridge axis and especially at FFS/BB, west of and at Nihoa I., around the islands of Kauai, Niihau, and Kaula, and in the eastern KC. Inversions tend to be absent far from the ridge and at gaps in the ridge. The difference in average K_ρ inside and outside of inversions indicates that large mixing events tend to occur when internal wave shears are enhanced.

Acknowledgments. This work was supported by the National Science Foundation under Grants OCE 98-19521 and 98-19530. The authors would like to acknowledge the contributions of Glenn Carter and Luc Rainville to the Doppler sonar data processing software. Lloyd Regier made sure SeaSoar worked at sea. Discussions with Robert Pinkel, Eric Kunze, Jody Klymak, and Jennifer MacKinnon were helpful.

Appendix

Procedure for Estimating the Turbulent Dissipation Rate of Kinetic Energy

The $\varepsilon_{\mathrm{IW1}}$ estimate of the turbulent dissipation rate of kinetic energy is computed using:

$$\varepsilon_{\mathrm{IW1}} = 6.73 \times 10^{-10} \left(\frac{N}{N_0}\right)^2 \left(\frac{S^2_{\mathrm{OBS}}}{S^2_{\mathrm{GM}}}\right)^2 \qquad [\mathrm{W\ kg^{-1}}] \tag{A. 1}$$

with $N_0 = 5.24 \times 10^{-3}$ rad s^{-1} (Gregg 1989). Eq. A. 1 applies to the thermocline. The mixed layer depth during the survey was typically 50 to 75 m. Mixed layer depth is defined as the depth at which the potential density is 0.1 kg m^{-3} greater than the shallowest measurement. We compute $\varepsilon_{\mathrm{IW1}}$ only below 100 m depth. For the depth range in the thermocline covered one-hundred percent of the time by SeaSoar, 100-330 m, N is the local buoyancy frequency smoothed by averaging N^2 over 11 consecutive profiles, approximately 40 km. Useful data from the 50 kHz sonar extends to 550 m, so below 330 m we use an exponential fit to N from the average of three full-depth Hawaii Ocean Time Series (HOTS) profiles taken north of the Kauai Channel near the time of the survey. S^2_{GM} is defined by:

$$S^2_{\mathrm{GM}} \equiv \int_0^{k_c^{\mathrm{GM}}} \phi_S^{\mathrm{GM}}(k)dk \tag{A. 2}$$

where $\phi_S^{\mathrm{GM}}(k)$ is the Garrett-Munk GM76 (Cairns and Williams 1976) vertical wavenumber shear spectrum according to Gregg and Kunze (1991):

$$\phi_S^{\mathrm{GM}}(k) = \frac{12\pi^2 E b^3 N_0^2}{j_*} \frac{k^2}{(1+k/k_*)^2}. \tag{A. 3}$$

The cyclic vertical wavenumber is k and k_c^{GM} is the cutoff wavenumber of 0.1 cycles m^{-1}. S^2_{GM} is thus the total variance of shear contained in all wavenumbers less than

k_c^{GM}. The result of evaluating the integral is:

$$S_{\mathrm{GM}}^2 = \frac{12\pi^2 E b^3 N_0^2}{j_*} k_*^3 \left[\left(1 + \frac{k_c^{\mathrm{GM}}}{k_*}\right) - 2\ln\left(1 + \frac{k_c^{\mathrm{GM}}}{k_*}\right) - \frac{1}{\left(1 + \frac{k_c^{\mathrm{GM}}}{k_*}\right)} \right] \qquad [\mathrm{s}^{-2}] \tag{A. 4}$$

where $E = 6.3 \times 10^{-5}$, $b = 1300$ m, and $j_* = 3$ are the GM parameters and $k_* = (j_* N)/(2bN_0)$. Functionally, S_{GM}^2 varies from $0.725N^2$ at $N = 1 \times 10^{-4}$ rad s^{-1} to $0.625N^2$ at $N = 1 \times 10^{-2}$ rad s^{-1}. Observed N ranges from 1.2×10^{-2} rad s^{-1} at 100 m to 5×10^{-3} rad s^{-1} at 550 m. The quantity S_{OBS}^2 is the observed equivalent of S_{GM}^2, computed as the squared magnitude of first-difference shear multiplied by a correction factor c:

$$S_{\mathrm{OBS}}^2 = c\left[(\Delta u/\Delta z)^2 + (\Delta v/\Delta z)^2\right] \qquad [\mathrm{s}^{-2}]. \tag{A. 5}$$

The difference interval Δz is the vertical grid spacing of 6.15 m discussed in Sec. 2 and u and v are, respectively, the east and north components of velocity from the Doppler sonar. First-differencing and Doppler sonar range-averaging both attenuate higher-wavenumber shear variance. The correction factor compensates for this loss of variance and is computed using:

$$c = \frac{S_{\mathrm{GM}}^2}{\int_0^{k_c^{\mathrm{GM}}} \phi_S^{\mathrm{GM}}(k)\, |F_{\mathrm{RA}}(k)|^2 \,\mathrm{sinc}^2(k\Delta z) dk} \tag{A. 6}$$

following Wijesekera *et al.* (1993) and Gregg and Sanford (1988). Assumed in Eq. A. 6 is that the observed shear spectrum has the same shape as the GM shear spectrum. The integral in Eq. A. 6 is evaluated numerically. The sinc^2 factor is the result of first-differencing. Over any listening interval a Doppler sonar echo is a weighted mean of reflections from a range of depths. For the Revelle Doppler sonar, the weighting is trapezoidal with approximately two-thirds of the data used in the mean for one bin contributing to the mean in the next bin. The range-averaging filter is given by:

$$F_{\mathrm{RA}}(k) = \frac{[\cos(a(Q+1)k) - \cos(a(3Q-1)k)]}{(2ak)Q(Q-1)} \tag{A. 7}$$

with $a = \pi c_s \tau \cos(\pi/6)$. $Q = 11$ and $\tau = 4.8 \times 10^{-4}$ s for the 50 kHz sonar, and $c_s = 1480$ m s^{-1} is the speed of sound. $F_{\mathrm{RA}}(k)$ and these values are specific to the Revelle Doppler sonar and are not discussed further. The correction factor varies from $c = 3.9$ at 550 m to $c = 4.4$ at 100 m.

A second method to estimate the turbulent dissipation rate was developed (Kunze *et al.* 1992; Polzin *et al.* 1995; Kunze and Sanford 1996; Gregg *et al.* 2003) in response to the criticism of Gargett (1990) that Gregg (1989) did not consider observed shear spectra with cutoff vertical wavenumber different from the cutoff in GM. We use the revised method as it is presented in Gregg *et al.* (2003). The second estimate is given by:

$$\varepsilon_{\mathrm{IW2}} = 6.73 \times 10^{-10} \left(\frac{N}{N_0}\right)^2 \left(\frac{\langle \phi_S^{\mathrm{OBS}}(k)\rangle}{\langle \phi_S^{\mathrm{GM}}(k)\rangle}\right)^2 \qquad [\mathrm{W\ kg^{-1}}] \tag{A. 8}$$

where:

$$\langle \phi_S^{\mathrm{OBS}}(k)\rangle \equiv \frac{1}{(k_c^{\mathrm{OBS}} - k_{min})} \int_{k_{min}}^{k_c^{\mathrm{OBS}}} \phi_S^{\mathrm{OBS}}(k)dk \tag{A. 9}$$

is the mean of the observed vertical wavenumber shear spectrum from the lowest resolved wavenumber k_{min} to a cutoff wavenumber k_c^{OBS} and:

$$\langle \phi_S^{\mathrm{GM}}(k)\rangle \equiv \frac{S_{\mathrm{GM}}^2}{(k_c^{\mathrm{GM}} - k_{min})}. \tag{A. 10}$$

k_c^{OBS} is defined by:

$$\int_{k_{min}}^{k_c^{\mathrm{OBS}}} \phi_S^{\mathrm{OBS}}(k)dk = S_{\mathrm{GM}}^2. \tag{A. 11}$$

That is, k_c^{OBS} is the wavenumber at which the variance in the observed spectrum equals the variance in the GM spectrum up to its rolloff wavenumber. The inclusion of the contribution to S_{GM}^2 from interval 0 to k_{min} causes negligible error as it is less than 0.5% of the total S_{GM}^2. Combining Eqs. A. 8-A. 11:

$$\varepsilon_{\mathrm{IW2}} = 6.73 \times 10^{-10} \left(\frac{N}{N_0}\right)^2 \left(\frac{(k_c^{\mathrm{GM}} - k_{min})}{(k_c^{\mathrm{OBS}} - k_{min})}\right)^2 \qquad [\mathrm{W\ kg^{-1}}]. \tag{A. 12}$$

The procedure for computing the observed shear spectrum $\phi_S^{\rm OBS}(k)$ to obtain $k_c^{\rm OBS}$ is as follows. A vertical trend is removed from each u and v profile and the vertical wavenumber periodogram is computed for each. Each periodogram is divided by $|F_{\rm RA}(k)|^2$ to correct for range-averaging. The velocity component spectra $\phi_u^{\rm OBS}(k)$ and $\phi_v^{\rm OBS}(k)$ are then computed by applying the horizontal mean $\{\}$ (discussed in Sec. 3a) to the periodograms. The shear spectra are determined using:

$$\phi_S^{\rm OBS}(k) = (2\pi k)^2 \left(\phi_u^{\rm OBS}(k) + \phi_v^{\rm OBS}(k)\right) \tag{A. 13}$$

The shear spectra are then integrated to determine $k_c^{\rm OBS}$, the wavenumber at which the integral equals $S_{\rm GM}^2$. The N used in calculating $\varepsilon_{\rm IW2}$ is from the vertical mean of the N^2 used for $\varepsilon_{\rm IW1}$. Gregg *et al.* (2003) apply two factors to $\varepsilon_{\rm IW2}$ to determine their full definition of the dissipation rate:

$$\varepsilon_{\rm GSW} = \varepsilon_{\rm IW2} G(R) L(\theta, N). \tag{A. 14}$$

We do not show results for $\varepsilon_{\rm GSW}$. The factor $G(R)$ is a result from Polzin *et al.* (1995) accounting for observations made in an internal wave field with frequency spectra of non-GM shape and is given by:

$$G(R) = \left(\frac{1 + 1/R}{4/3}\right)\left(\frac{2}{R-1}\right)^{1/2} \tag{A. 15}$$

where:

$$R = \frac{\frac{1}{N^2}\int_0^{k_c^{\rm OBS}} \phi_S^{\rm OBS}(k)dk}{\int_0^{k_c^{\rm OBS}} \phi_{\eta_z}^{\rm OBS}(k)dk}. \tag{A. 16}$$

The denominator is the strain (η_z) variance where η is the isopycnal displacement. For our data, η is a perturbation from the same horizontal mean as used in computing the velocity component spectra. The strain spectrum is computed in the same way as the shear spectra. $G(R)$ equals 1 when R has the GM value of 3. The latitude (θ)

dependence factor is given by:

$$L(\theta, N) = \frac{f(\theta)\cosh^{-1}(N/f(\theta))}{f(30^\circ)\cosh^{-1}(N_0/f(30^\circ))}. \quad \text{(A. 17)}$$

Across observations from a number sites, Gregg *et al.* (2003) find that $\varepsilon_{\mathrm{IW2}}$ has the largest range and is the most important among the factors in Eq. A. 14.

There is uncertainty in our estimate of the turbulent dissipation rate because of the difference between $\varepsilon_{\mathrm{IW1}}$ and $\varepsilon_{\mathrm{IW2}}$ and $\varepsilon_{\mathrm{GSW}}$. In Sec. 3 good agreement is found between estimates $\varepsilon_{\mathrm{IW1}}$ and $\varepsilon_{\mathrm{IW2}}$. However, estimate $\varepsilon_{\mathrm{GSW}}$ gives lesser values. The observed range of R is 7 to 18 and the corresponding range of $G(R)$ is 0.5 to 0.3. The observed range of R indicates that the dominant frequency contributing to shear and strain at Hawaii is closer to inertial than the corresponding GM frequency (with $R = 3$). For the frequency of the M_2 tide, R at Hawaiian latitudes is about 1.4. $L(\theta, N)$ is approximately 0.8. Therefore, $\varepsilon_{\mathrm{IW1}}$ and $\varepsilon_{\mathrm{IW2}}$ are overestimates relative to $\varepsilon_{\mathrm{GSW}}$ by at worst a factor of $1/[G(R)L(\theta, N)] = 1/[0.3 \times 0.8] \approx 4$. We show results for $\varepsilon_{\mathrm{IW1}}$ and $\varepsilon_{\mathrm{IW2}}$. Simultaneous microstructure measurements were not made, so ε cannot be determined independently, and we cannot determine whether $\varepsilon_{\mathrm{GSW}}$ is a better estimate. The emphasis is on across- and along-ridge structure and not on absolute magnitudes.

References

Alford, M.H. and R. Pinkel, 2000a: Observations of overturning in the thermocline: the context of ocean mixing. *J. Phys. Oceanogr.*, **30**, 805–832.

Althaus, A.M., E. Kunze, and T.B. Sanford, 2003: Internal tide radiation from Mendocino Escarpment. *J. Phys. Oceanogr.*, **33**, 1510–1527.

Cairns, J.L. and G.O. Williams, 1976: Internal wave observations from a midwater float, 2. *J. Geophys. Res.*, **81(12)**, 1943–1950.

Davis, R.E., 1994a: Diapycnal mixing in the ocean: equations for large-scale budgets. *J. Phys. Oceanogr.*, **24**, 777–800.

Dillon, T.M., 1982: Vertical overturns: A comparison of Thorpe and Ozmidov scales. *J. Geophys. Res.*, **87**, 9601–9613.

Egbert, G.D. and R.D. Ray, 2000: Significant dissipation of tidal energy in the deep ocean inferred from satellite altimeter data. *Nature*, **405**, 775–778.

Galbraith, P.S. and D.E. Kelley, 1996: Identifying overturns in CTD profiles. *J. Atmos. Oceanic Technol.*, **13**, 688–702.

Gargett, A.E., 1990: Do we really know how to scale the turbulent kinetic energy dissipation rate ε due to breaking of oceanic internal waves?. *J. Geophys. Res.*, **95(C9)**, 15971–15974.

Gregg, M.C., 1987: Diapycnal mixing in the thermocline: a review. *J. Geophys. Res.*, **92**, 5249–5286.

Gregg, M.C., 1989: Scaling turbulent dissipation in the thermocline. *J. Geophys. Res.*, **94**, 9686–9698.

Gregg, M.C. and E. Kunze, 1991: Shear and strain in Santa Monica basin. *J. Geophys. Res.*, **96(C9)**, 16709–16719.

Gregg, M.C. and T.B. Sanford, 1988: The dependence of turbulent dissipation on stratification in a diffusively stable thermocline. *J. Geophys. Res.*, **93(C10)**, 12381–12392.

Gregg, M.C., T.B. Sanford, and D.P. Winkel, 2003: Reduced mixing from the breaking of internal waves in equatorial waters. *Nature*, **422**, 513–515.

Henyey, F.S., J. Wright, and S.M. Flatté, 1986: Energy and action flow through the internal wave field: an eikonal approach. *J. Geophys. Res.*, **91(C7)**, 8487–8495.

Klymak, J.M., J.N. Moum, J.D. Nash, E.B. Kunze, J.B. Girton, Glenn S. Carter, C. Lee, T.B. Sanford, and M.C. Gregg, 2005: An estimate of energy lost to turbulence at the Hawaiian Ridge. *J. Phys. Oceanogr.*, submitted.

Kunze, E., M.A. Kennelly, and T.B. Sanford, 1992: The depth dependence of shear finestructure off Point Arena and near Pioneer Seamount. *J. Phys. Oceanogr.*, **22**, 29–41.

Kunze, E. and T.B. Sanford, 1996: Abyssal mixing: where it is not. *J. Phys. Oceanogr.*, **26**, 2286–2296.

Kunze, E. and J.M. Toole, 1997: Tidally driven vorticity, diurnal shear, and turbulence atop Fieberling Seamount. *J. Phys. Oceanogr.*, **27**, 2663–2693.

Ledwell, J.R., A.J. Watson, and C.S. Law, 1993: Evidence of slow mixing across the pycnocline from an open-oean tracer release experiment. *Nature*, **364**, 701–703.

Lee, Craig M., E. Kunze, T.B. Sanford, J.D. Nash, M.A. Merrifield, and P.E. Holloway, 2005: Internal tides and turbulence along the 3000-m isobath of the Hawaiian Ridge with model comparisons. *J. Phys. Oceanogr.*, submitted.

Lueck, R.G. and T.D. Mudge, 1997: Topographically induced mixing around a shallow seamount. *Science*, **276**, 1831–1833.

Martin, J.P., D.L. Rudnick, and R. Pinkel, 2005: Spatially broad observations of internal waves in the upper ocean at the Hawaiian Ridge. *J. Phys. Oceanogr.*, accepted.

Merrifield, M.A. and P.E. Holloway, 2002: Model estimates of M_2 internal tide energetics at the Hawaiian Ridge. *J. Geophys. Res.*, **107(C8)**, 3179, doi:10.1029/2001JC000996.

Munk, W. and C. Wunsch, 1998: Abyssal recipes II: energetics of tidal and wind mixing. *Deep-Sea Res.*, **45**, 1977–2010.

Osborn, T.R., 1980: Estimates of the local rate of vertical diffusion from dissipation measurements. *J. Phys. Oceanogr.*, **10**, 83–89.

Polzin, K.L., J.M. Toole, and R.W. Schmitt, 1995: Finescale parameterizations of turbulent dissipation. *J. Phys. Oceanogr.*, **25**, 306–328.

Rudnick, D.L. and Coauthors, 2003: From tides to mixing along the Hawaiian Ridge. *Science*, **301**, 355–357.

Thorpe, S.A., 1978: On the shape and breaking of finite amplitude internal gravity waves in a shear flow. *J. Fluid Mech.*, **85(1)**, 7–31.

Toole, J.M., K.L. Polzin, and R.W. Schmitt, 1994: Estimates of diapycnal mixing in the abyssal ocean. *Science*, **264**, 1120–1123.

Ullman, D.S., A.C. Dale, D. Hebert, and J.A. Barth, 2003: The front on the northern flank of Georges Bank in spring: 2. cross-fronal fluxes and mixing. *J. Geophys. Res.*, **108(C11)**, doi:10.1029/2002JC001328.

Wijesekera, H., L. Padman, T. Dillon, M. Levine, C. Paulson, and R. Pinkel, 1993: The application of internal-wave dissipation models to a region of strong mixing. *J. Phys. Oceanogr.*, **23**, 269–286.

Wunsch, C. and R. Ferrari, 2004: Vertical mixing, energy, and the general circulation of the oceans. *Ann. Rev. Fluid Mech.*, **36**, 281–314.

Zaron, E.D. and G.D. Egbert, 2005: Estimating Open-Ocean Barotropic Tidal Dissipation: The Hawaiian Ridge. *J. Phys. Oceanogr.*, submitted.

Table Captions

Table 1: In the upper half of the table are estimates of the across-ridge gradients of $\log_{10}(\langle\{\varepsilon_{\mathrm{IW1}}\}\rangle_{\mathrm{d}})$, $\log_{10}(\langle\{\varepsilon_{\mathrm{IW2}}\}\rangle_{\mathrm{d}})$, $\log_{10}(\langle\{K_\rho(\varepsilon_{\mathrm{IW1}})\}\rangle_{\mathrm{d}})$, and $\log_{10}(\langle\{K_\rho(\varepsilon_{\mathrm{IW2}})\}\rangle_{\mathrm{d}})$ per 100 km at KC and FFS/BB. Values shown are from the exponential fits discussed in the text and shown in Figs. 3 and 4. The fits are from position -170 km to the position of maximum value and from the maximum value to 170 km at KC, and from -120 km to the maximum value at FFS/BB. The signs of the gradients indicate decay away from the maxima. In the lower half of the table are the e-folding length scales of the fits to ε and K_ρ in km.

Figure Captions

Figure 1: The cruise track for the September 2000 HOME SeaSoar / Doppler sonar survey is shown with a solid black line. The repeated across-ridge track is shown with a dashed line. In the main text, the Kauai Channel (KC) designation refers to the region and tracks between the islands of Kauai and Oahu. Niihau is the island just southwest of (22°N,160°W) and Kaula is the small island just southwest of Niihau. Nihoa is a small island just east of 162°W. Brooks Banks (BB) and French Frigate Shoals (FFS) are broad regions with bottom depths less than 500 m.

Figure 2: Sections of $\log_{10}(K_\rho(\varepsilon_{\mathrm{IW1}}))$ from south of Kauai I. to south of Oahu I. at (a) the peak of spring tide and at (b) the end of neap tide. The cruisetrack arcs across the KC (Fig. 1) and the peaks in bathymetry (c) are the southwest slope of Oahu I. and the south slope of Kauai I.. The pink circles indicate where an M_2 internal tide ray directed across-ridge intersects this section (see text). At spring tide, values of

$K_\rho(\varepsilon_{\mathrm{IW1}})$ in excess of 10^{-3} m^2 s^{-1} are typical for over 200 m above the ray.

Figure 3: Mean-square (ms) shear magnitude, mean turbulent dissipation rate of kinetic energy, and mean diapycnal eddy diffusivity as functions of across-ridge position at KC. The position axis is parallel to the across-ridge survey tracks at KC. Positive positions are on the north side of the ridge. (a) The ms shear magnitude, $\langle\{S^2\}\rangle_{\mathrm{d}}$. The $\{\}$ operator is an across-ridge mean over bins 10 km wide in position normal to the ridge, centered at the positions shown in the figure. The $\langle\rangle_{\mathrm{d}}$ operator is a mean over depths 100-550 m. (b) $\langle\{\varepsilon_{\mathrm{IW1}}\}\rangle_{\mathrm{d}}$ (blue -□-) and $\langle\{\varepsilon_{\mathrm{IW2}}\}\rangle_{\mathrm{d}}$ (red -+-). The dashed lines are exponential function fits to $\langle\{\varepsilon_{\mathrm{IW1}}\}\rangle_{\mathrm{d}}$ and $\langle\{\varepsilon_{\mathrm{IW2}}\}\rangle_{\mathrm{d}}$ from position -170 km to the maximum of each estimate and from the maximum to position 170 km. (c) $\langle\{K_\rho(\varepsilon_{\mathrm{IW1}})\}\rangle_{\mathrm{d}}$ (blue -□-) and $\langle\{K_\rho(\varepsilon_{\mathrm{IW2}})\}\rangle_{\mathrm{d}}$ (red -+-). The dashed lines are exponential fits computed as in (b). (d) $\log_{10}(\{K_\rho(\varepsilon_{\mathrm{IW1}})\})$.

Figure 4: Mean-square (ms) shear magnitude, mean turbulent dissipation rate of kinetic energy, and mean diapycnal eddy diffusivity as functions of across-ridge position at FFS/BB. The position axis is parallel to the across-ridge survey tracks at FFS/BB. Positive positions are on the north side of the ridge. (a) The ms shear magnitude, $\langle\{S^2\}\rangle_{\mathrm{d}}$. The $\{\}$ operator is an across-ridge mean over bins 10 km wide in position normal to the ridge, centered at the positions shown in the figure. The $\langle\rangle_{\mathrm{d}}$ operator is a mean over depths 100-550 m. (b) $\langle\{\varepsilon_{\mathrm{IW1}}\}\rangle_{\mathrm{d}}$ (blue -□-) and $\langle\{\varepsilon_{\mathrm{IW2}}\}\rangle_{\mathrm{d}}$ (red -+-). The dashed lines are exponential function fits to $\langle\{\varepsilon_{\mathrm{IW1}}\}\rangle_{\mathrm{d}}$ and $\langle\{\varepsilon_{\mathrm{IW2}}\}\rangle_{\mathrm{d}}$ from position -120 km to the maximum of each estimate and from the maximum to position 120 km. (c) $\langle\{K_\rho(\varepsilon_{\mathrm{IW1}})\}\rangle_{\mathrm{d}}$ (blue -□-) and $\langle\{K_\rho(\varepsilon_{\mathrm{IW2}})\}\rangle_{\mathrm{d}}$ (red -+-). The dashed lines are exponential fits computed as in (b). (d) $\log_{10}(\{K_\rho(\varepsilon_{\mathrm{IW1}})\})$.

Figure 5: A map of $\log_{10}(\langle\varepsilon_{\mathrm{IW1}}\rangle_b)$ where $\langle\rangle_b$ is a mean over all profiles that fall within regularly-spaced 20 km × 20 km boxes and over the depth range 100-550 m. Observations from the entire cruise track shown in Fig. 1 are used.

Figure 6: A map of $\log_{10}(\langle K_\rho(\varepsilon_{\mathrm{IW1}})\rangle_b)$ where $\langle\rangle_b$ is a mean over all profiles that fall within regularly-spaced 20 km × 20 km boxes and over the depth range 100-550 m. Observations from the entire cruisetrack shown in Fig. 1 are used.

Figure 7: The values shown are integrals of $\{\rho\}\{\varepsilon\}$ over the depth range 100-550 m and across-ridge from the ridge peak outwards to each position x. Two estimates of ε are used: $\varepsilon_{\mathrm{IW1}}$ (-□-) and $\varepsilon_{\mathrm{IW2}}$ (-+-). The integrals in panel (a) are for KC and the integrals in (b) are for FFS/BB.

Figure 8: Examples of inversions in potential density (σ_θ) profiles with large depth extent are shown by the solid curves. The potential density profiles sorted to be statically stable ($\hat{\sigma_\theta}$) are shown by the dashed curves. The positions of the individual profiles are: (a) (23.12°N,163.15°W), west of Nihoa I. in the first along-ridge survey, (b) (22.91°N,162.00°W), south of Nihoa I. in the second along-ridge survey, (c) (21.30°N,158.66°W), 42 km from the ridge at KC, and (d) (21.60°N,160.55°W), near Kaula I.

Figure 9: Probability density functions of (a) log Thorpe scale $\log_{10}(L_{\mathrm{T}})$, (b) log inversion height $\log_{10}(L_{\mathrm{Z}})$, and (c) log mean inversion buoyancy frequency $\log_{10}(\overline{N})$ for all accepted inversions below the mixed layer.

Figure 10: A map of the mean inversion height L_{Z} where the mean is over all inversions below 100 m depth that fall within the boxes of Fig. 5.

Figure 11: A map of the fraction of occurrence of inversions. The fraction is the sum of L_{Z} over all inversions in each box (boxes defined for Fig. 5) divided by the sum of available depth ranges over all profiles in that box. Simply, it is the mean fraction of the water column that is inverted. The majority of displayed boxes contain one inversion, but one box centered at (23.15°N,163.11°W) contains 14 and several near the ridge in the eastern KC contain more than 5.

Figure 12: Probability density functions of $\log_{10}(K_\rho(\varepsilon_{\mathrm{IW1}}))$ outside and inside density

inversions in the depth range from 100 m to the bottom of the SeaSoar profiles. The range of each bin includes all values that would be considered the same order of magnitude. For example, the range of the fourth bin is 5×10^{-6} to 5×10^{-5} $\mathrm{m^2\ s^{-1}}$. The first bin, however, contains contributions from a long tail extending several orders of magnitude lower. Values of order 10^{-4} and 10^{-3} $\mathrm{m^2\ s^{-1}}$ occur more frequently inside inversions than outside inversions.

	KC	KC	FFS/BB
across-ridge gradient of:	-170 - max.	max. - 170	-120 - max.
$\log_{10}(\langle\{\varepsilon_{\mathrm{IW1}}\}\rangle_{\mathrm{d}})$ (W kg^{-1}/100 km)	0.59	-0.29	0.52
$\log_{10}(\langle\{\varepsilon_{\mathrm{IW2}}\}\rangle_{\mathrm{d}})$ (W kg^{-1}/100 km)	0.38	-0.29	0.68
$\log_{10}(\langle\{K_\rho(\varepsilon_{\mathrm{IW1}})\}\rangle_{\mathrm{d}})$ (m^2 s^{-1}/100 km)	0.58	-0.30	0.54
$\log_{10}(\langle\{K_\rho(\varepsilon_{\mathrm{IW2}})\}\rangle_{\mathrm{d}})$ (m^2 s^{-1}/100 km)	0.42	-0.26	0.67
e-folding length scale of:			
$\varepsilon_{\mathrm{IW1}}$ (km)	74	148	84
$\varepsilon_{\mathrm{IW2}}$ (km)	113	150	64
$K_\rho(\varepsilon_{\mathrm{IW1}})$ (km)	76	147	80
$K_\rho(\varepsilon_{\mathrm{IW2}})$ (km)	103	166	64

Table 1: In the upper half of the table are estimates of the across-ridge gradients of $\log_{10}(\langle\{\varepsilon_{\mathrm{IW1}}\}\rangle_{\mathrm{d}})$, $\log_{10}(\langle\{\varepsilon_{\mathrm{IW2}}\}\rangle_{\mathrm{d}})$, $\log_{10}(\langle\{K_\rho(\varepsilon_{\mathrm{IW1}})\}\rangle_{\mathrm{d}})$, and $\log_{10}(\langle\{K_\rho(\varepsilon_{\mathrm{IW2}})\}\rangle_{\mathrm{d}})$ per 100 km at KC and FFS/BB. Values shown are from the exponential fits discussed in the text and shown in Figs. 3 and 4. The fits are from position -170 km to the position of maximum value and from the maximum value to 170 km at KC, and from -120 km to the maximum value at FFS/BB. The signs of the gradients indicate decay away from the maxima. In the lower half of the table are the e-folding length scales of the fits to ε and K_ρ in km.

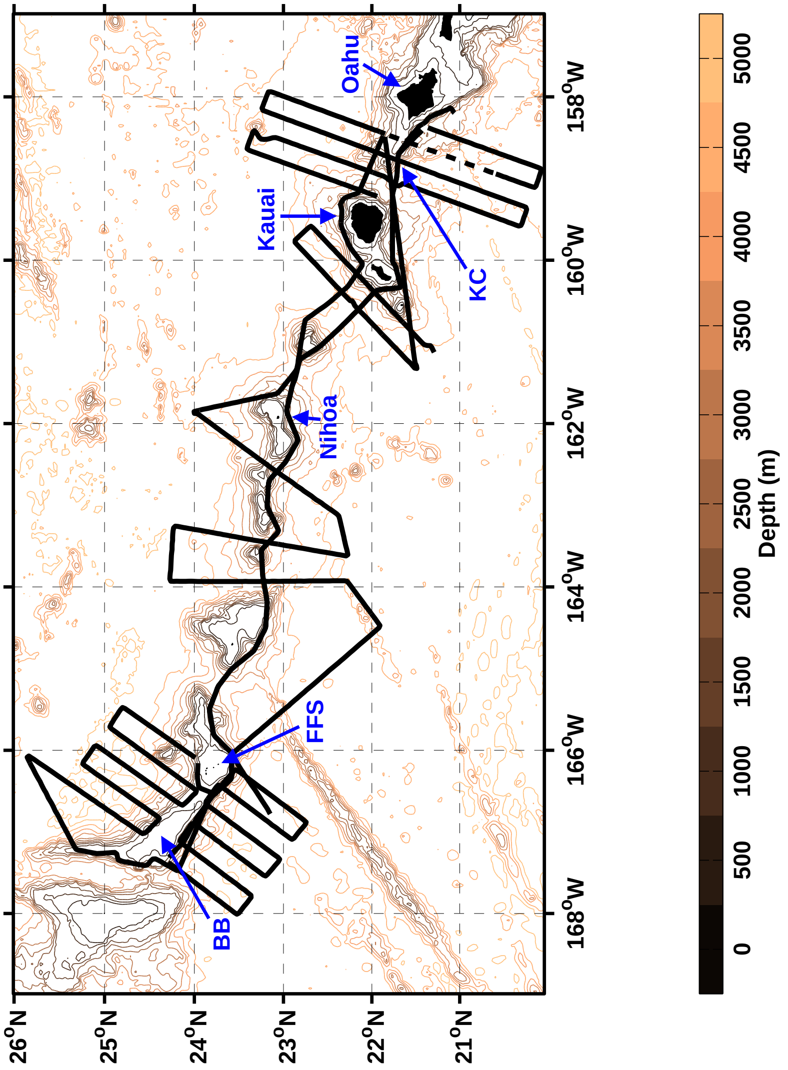

Figure 1: The cruise track for the September 2000 HOME SeaSoar / Doppler sonar survey is shown with a solid black line. The repeated across-ridge track is shown with a dashed line. In the main text, the Kauai Channel (KC) designation refers to the region and tracks between the islands of Kauai and Oahu. Niihau is the island just southwest of (22°N,160°W) and Kaula is the small island just southwest of Niihau. Nihoa is a small island just east of 162°W. Brooks Banks (BB) and French Frigate Shoals (FFS) are broad regions with bottom depths less than 500 m.

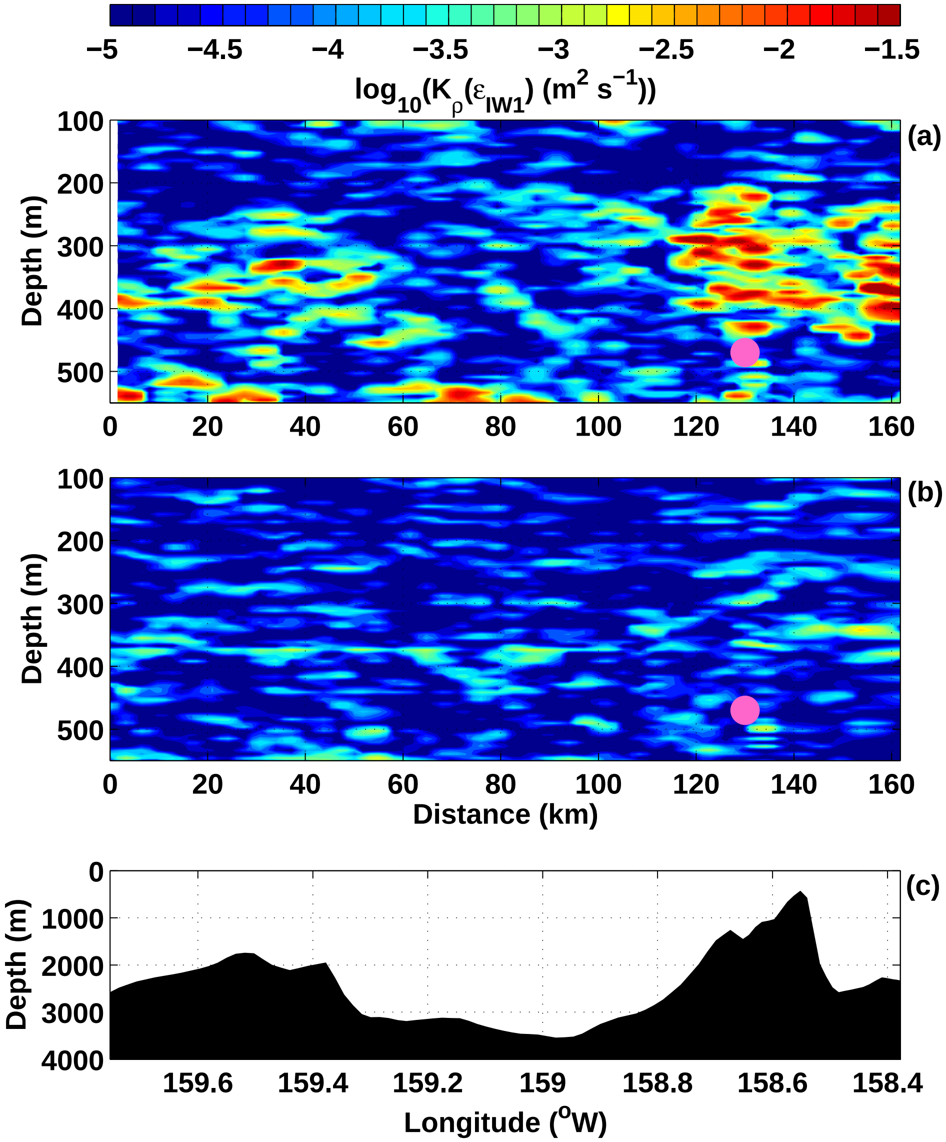

Figure 2: Sections of $\log_{10}(K_\rho(\varepsilon_{\mathrm{IW1}}))$ from south of Kauai I. to south of Oahu I. at (a) the peak of spring tide and at (b) the end of neap tide. The cruisetrack arcs across the KC (Fig. 1) and the peaks in bathymetry (c) are the southwest slope of Oahu I. and the south slope of Kauai I.. The pink circles indicate where an M_2 internal tide ray directed across-ridge intersects this section (see text). At spring tide, values of $K_\rho(\varepsilon_{\mathrm{IW1}})$ in excess of 10^{-3} m^2 s^{-1} are typical for over 200 m above the ray.

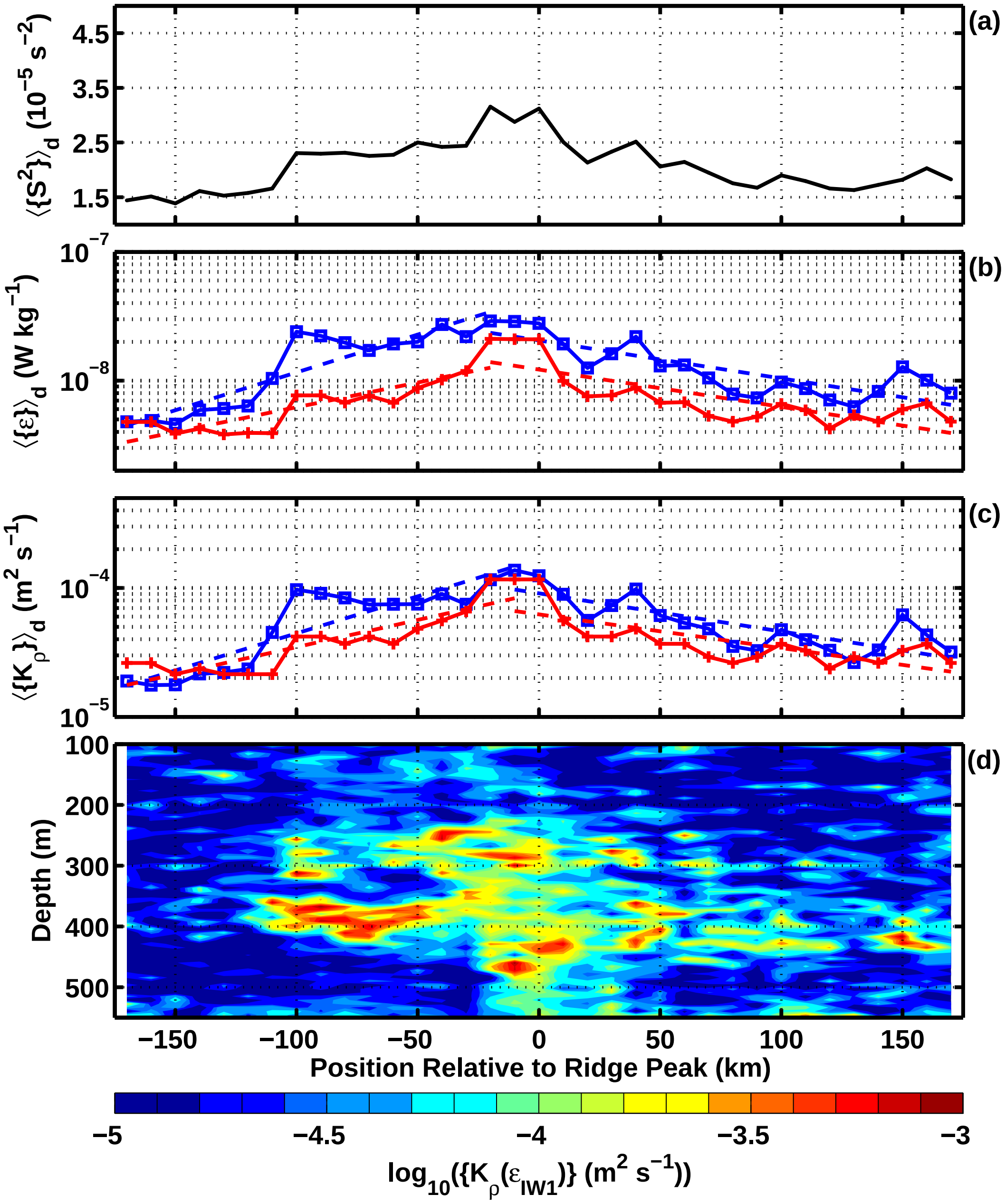

Figure 3: Mean-square (ms) shear magnitude, mean turbulent dissipation rate of kinetic energy, and mean diapycnal eddy diffusivity as functions of across-ridge position at KC. The position axis is parallel to the across-ridge survey tracks at KC. Positive positions are on the north side of the ridge. (a) The ms shear magnitude, $\langle\{S^2\}\rangle_{\mathrm{d}}$. The $\{\}$ operator is an across-ridge mean over bins 10 km wide in position normal to the ridge, centered at the positions shown in the figure. The $\langle\rangle_{\mathrm{d}}$ operator is a mean over depths 100-550 m. (b) $\langle\{\varepsilon_{\mathrm{IW1}}\}\rangle_{\mathrm{d}}$ (blue -□-) and $\langle\{\varepsilon_{\mathrm{IW2}}\}\rangle_{\mathrm{d}}$ (red -+-). The dashed lines are exponential function fits to $\langle\{\varepsilon_{\mathrm{IW1}}\}\rangle_{\mathrm{d}}$ and $\langle\{\varepsilon_{\mathrm{IW2}}\}\rangle_{\mathrm{d}}$ from position -170 km to the maximum of each estimate and from the maximum to position 170 km. (c) $\langle\{K_\rho(\varepsilon_{\mathrm{IW1}})\}\rangle_{\mathrm{d}}$ (blue -□-) and $\langle\{K_\rho(\varepsilon_{\mathrm{IW2}})\}\rangle_{\mathrm{d}}$ (red -+-). The dashed lines are exponential fits computed as in (b). (d) $\log_{10}(\{K_\rho(\varepsilon_{\mathrm{IW1}})\})$.

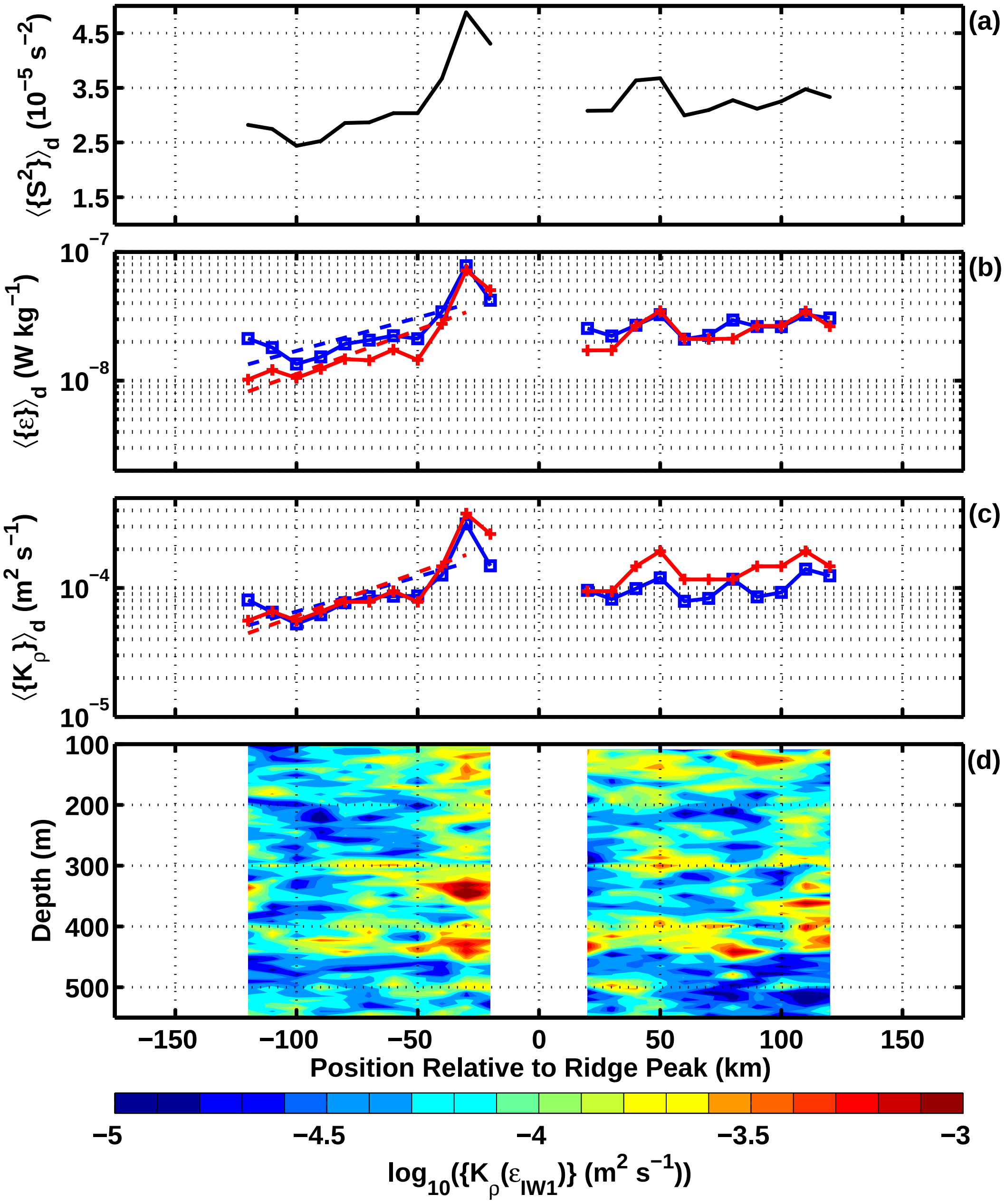

Figure 4: Mean-square (ms) shear magnitude, mean turbulent dissipation rate of kinetic energy, and mean diapycnal eddy diffusivity as functions of across-ridge position at FFS/BB. The position axis is parallel to the across-ridge survey tracks at FFS/BB. Positive positions are on the north side of the ridge. (a) The ms shear magnitude, $\langle\{S^2\}\rangle_{\mathrm{d}}$. The $\{\}$ operator is an across-ridge mean over bins 10 km wide in position normal to the ridge, centered at the positions shown in the figure. The $\langle\rangle_{\mathrm{d}}$ operator is a mean over depths 100-550 m. (b) $\langle\{\varepsilon_{\mathrm{IW1}}\}\rangle_{\mathrm{d}}$ (blue -□-) and $\langle\{\varepsilon_{\mathrm{IW2}}\}\rangle_{\mathrm{d}}$ (red -+-). The dashed lines are exponential function fits to $\langle\{\varepsilon_{\mathrm{IW1}}\}\rangle_{\mathrm{d}}$ and $\langle\{\varepsilon_{\mathrm{IW2}}\}\rangle_{\mathrm{d}}$ from position -120 km to the maximum of each estimate and from the maximum to position 120 km. (c) $\langle\{K_\rho(\varepsilon_{\mathrm{IW1}})\}\rangle_{\mathrm{d}}$ (blue -□-) and $\langle\{K_\rho(\varepsilon_{\mathrm{IW2}})\}\rangle_{\mathrm{d}}$ (red -+-). The dashed lines are exponential fits computed as in (b). (d) $\log_{10}(\{K_\rho(\varepsilon_{\mathrm{IW1}})\})$.

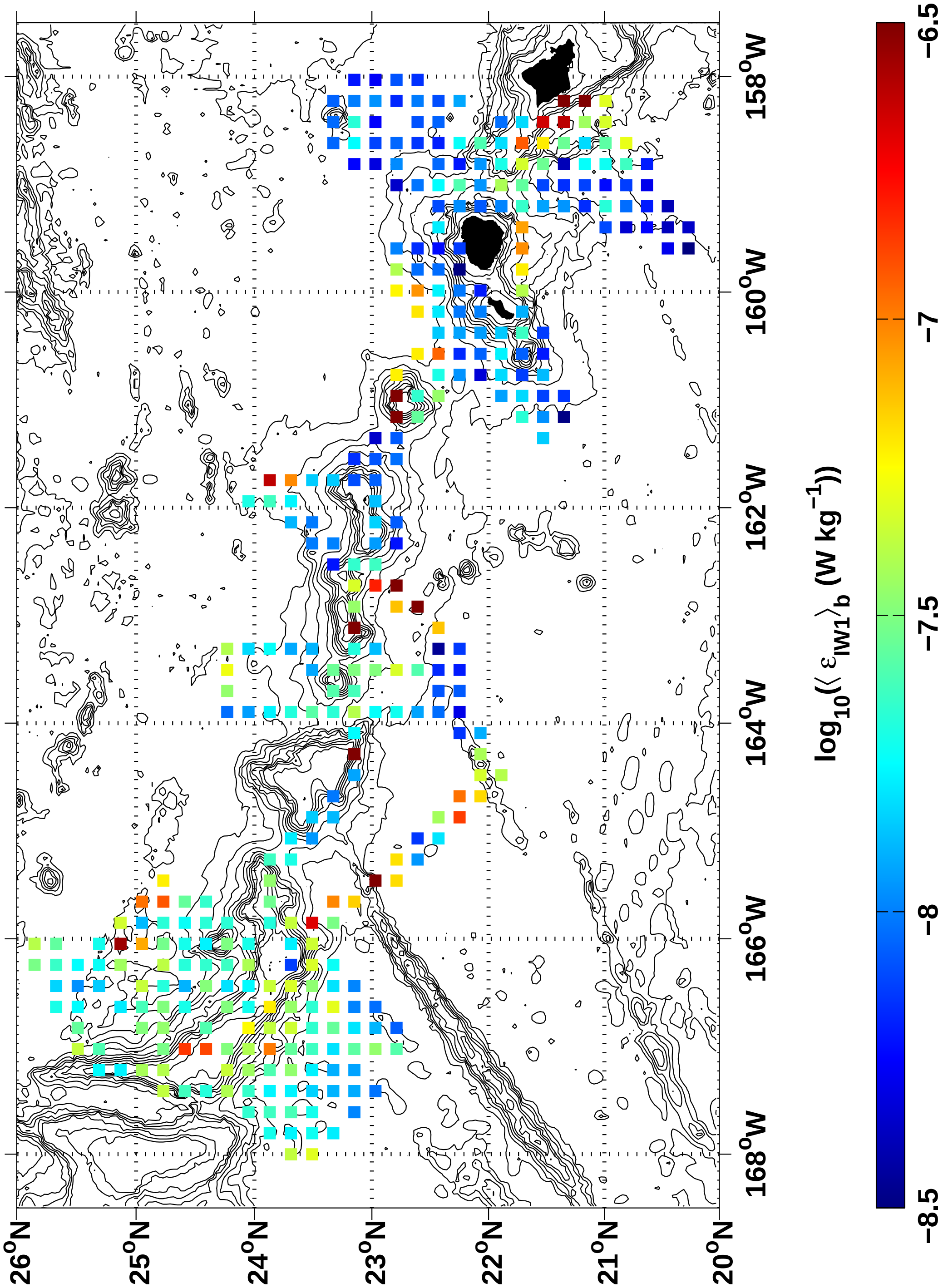

Figure 5: A map of $\log_{10}(\langle\varepsilon_{\mathrm{IW1}}\rangle_b)$ where $\langle\rangle_b$ is a mean over all profiles that fall within regularly-spaced 20 km × 20 km boxes and over the depth range 100-550 m. Observations from the entire cruise track shown in Fig. 1 are used.

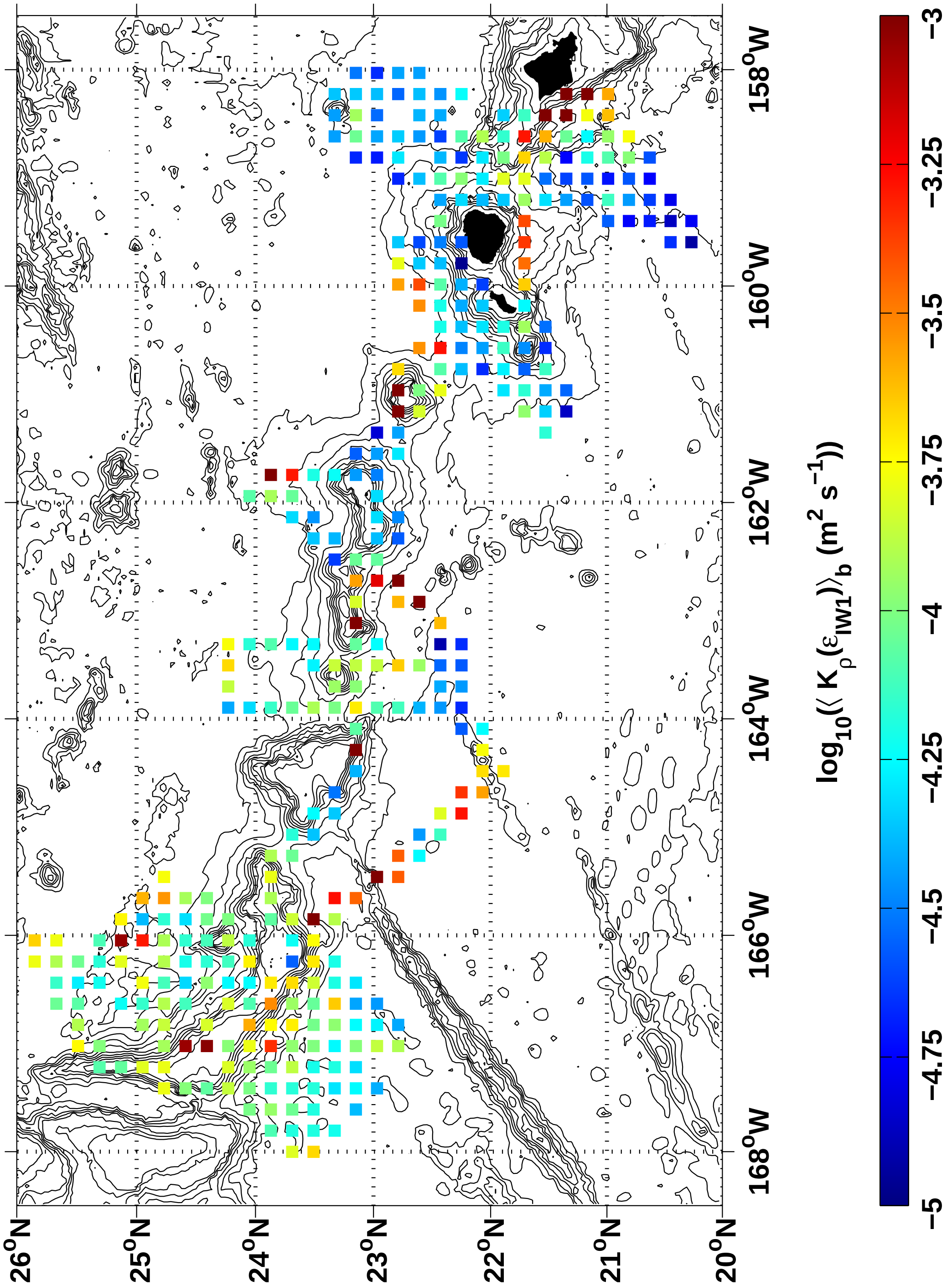

Figure 6: A map of $\log_{10}(\langle K_\rho(\varepsilon_{\mathrm{IW1}})\rangle_b)$ where $\langle\rangle_b$ is a mean over all profiles that fall within regularly-spaced 20 km × 20 km boxes and over the depth range 100-550 m. Observations from the entire cruisetrack shown in Fig. 1 are used.

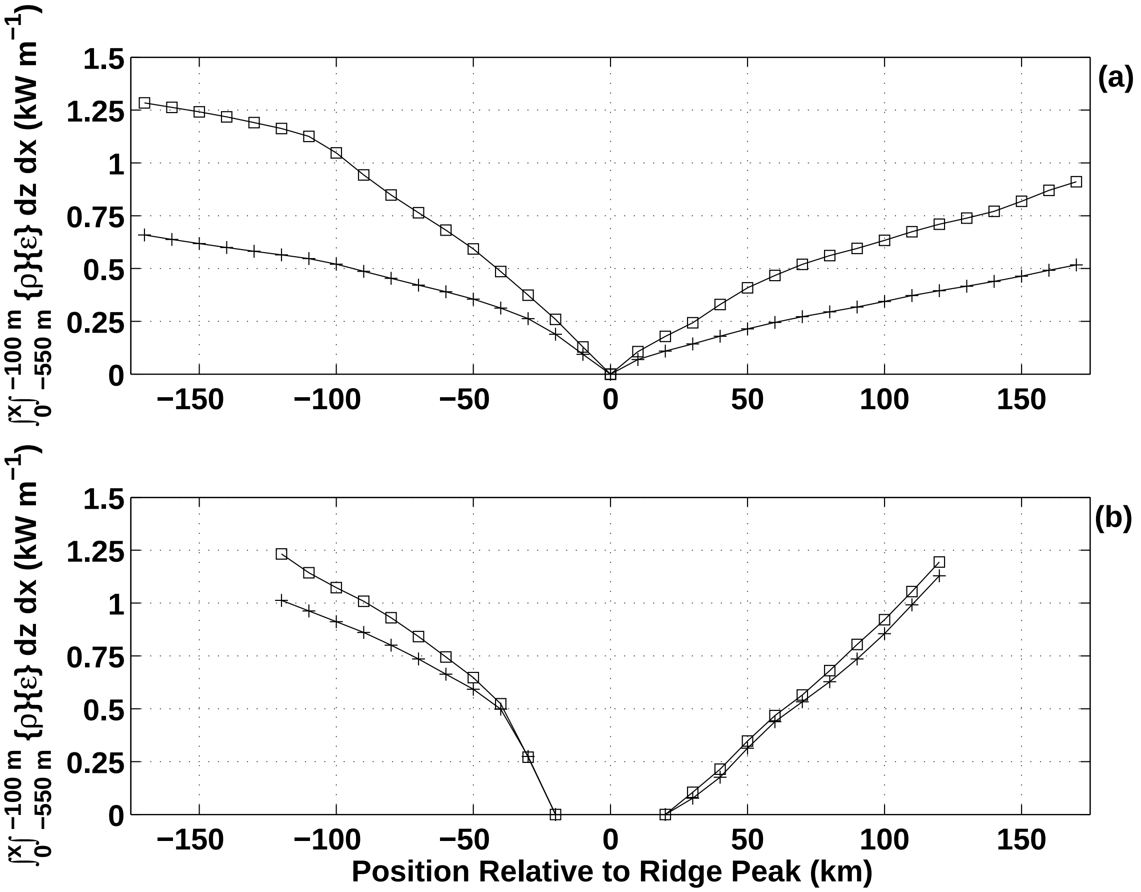

Figure 7: The values shown are integrals of $\{\rho\}\{\varepsilon\}$ over the depth range 100-550 m and across-ridge from the ridge peak outwards to each position x. Two estimates of ε are used: $\varepsilon_{\mathrm{IW1}}$ (-□-) and $\varepsilon_{\mathrm{IW2}}$ (-+-). The integrals in panel (a) are for KC and the integrals in (b) are for FFS/BB.

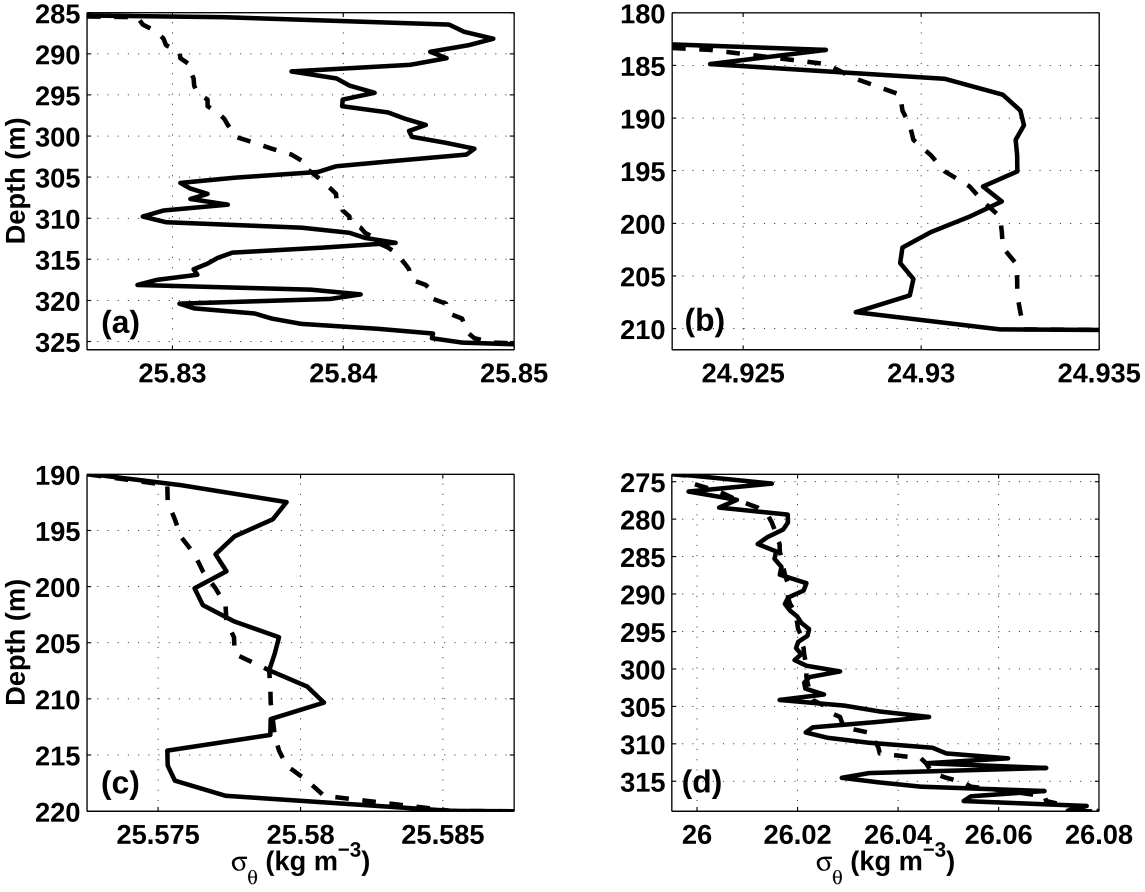

Figure 8: Examples of inversions in potential density (σ_θ) profiles with large depth extent are shown by the solid curves. The potential density profiles sorted to be statically stable ($\hat{\sigma_\theta}$) are shown by the dashed curves. The positions of the individual profiles are: (a) (23.12°N,163.15°W), west of Nihoa I. in the first along-ridge survey, (b) (22.91°N,162.00°W), south of Nihoa I. in the second along-ridge survey, (c) (21.30°N,158.66°W), 42 km from the ridge at KC, and (d) (21.60°N,160.55°W), near Kaula I.

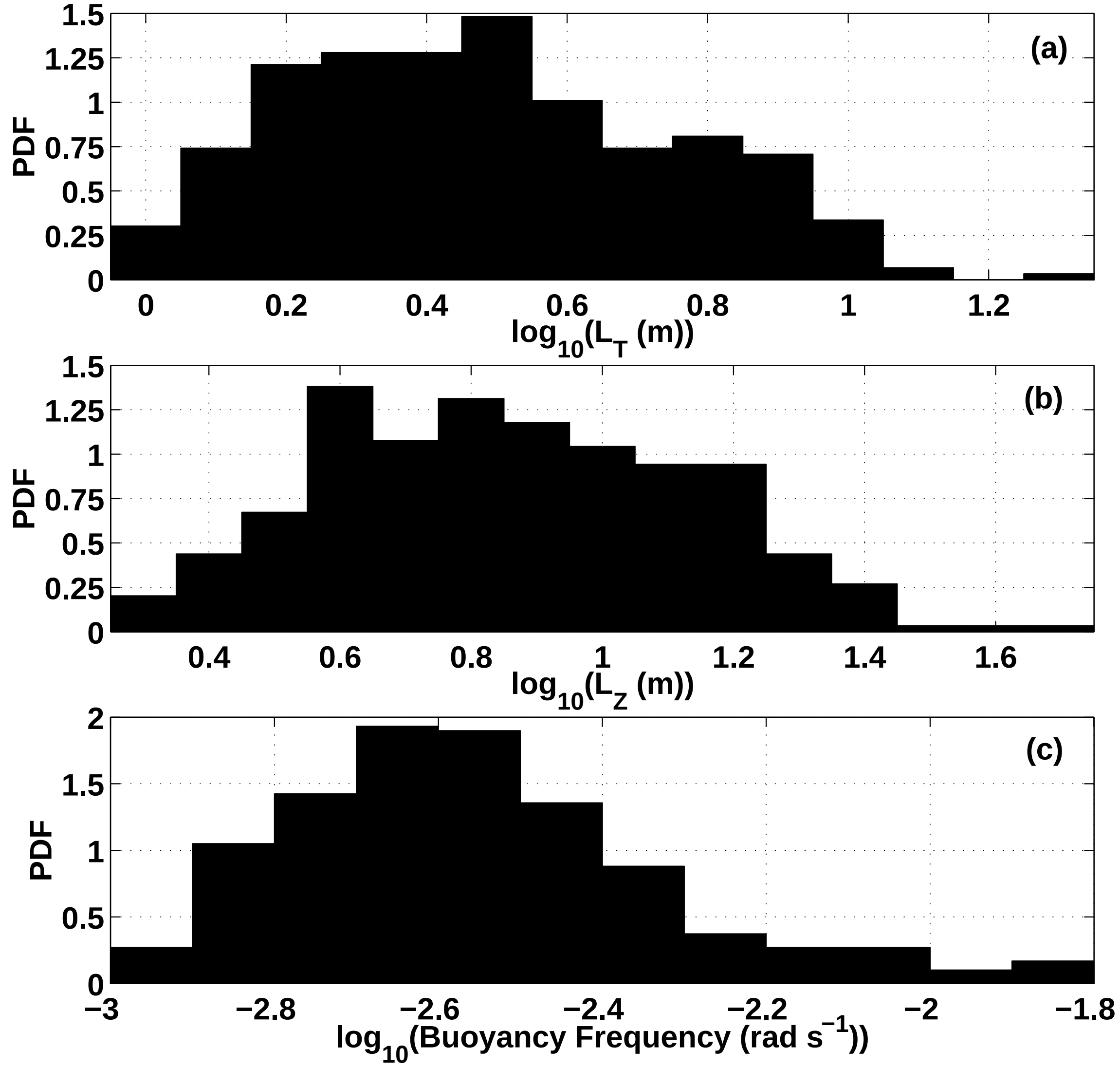

Figure 9: Probability density functions of (a) log Thorpe scale $\log_{10}(L_{\mathrm{T}})$, (b) log inversion height $\log_{10}(L_{\mathrm{Z}})$, and (c) log mean inversion buoyancy frequency $\log_{10}(\overline{N})$ for all accepted inversions below the mixed layer.

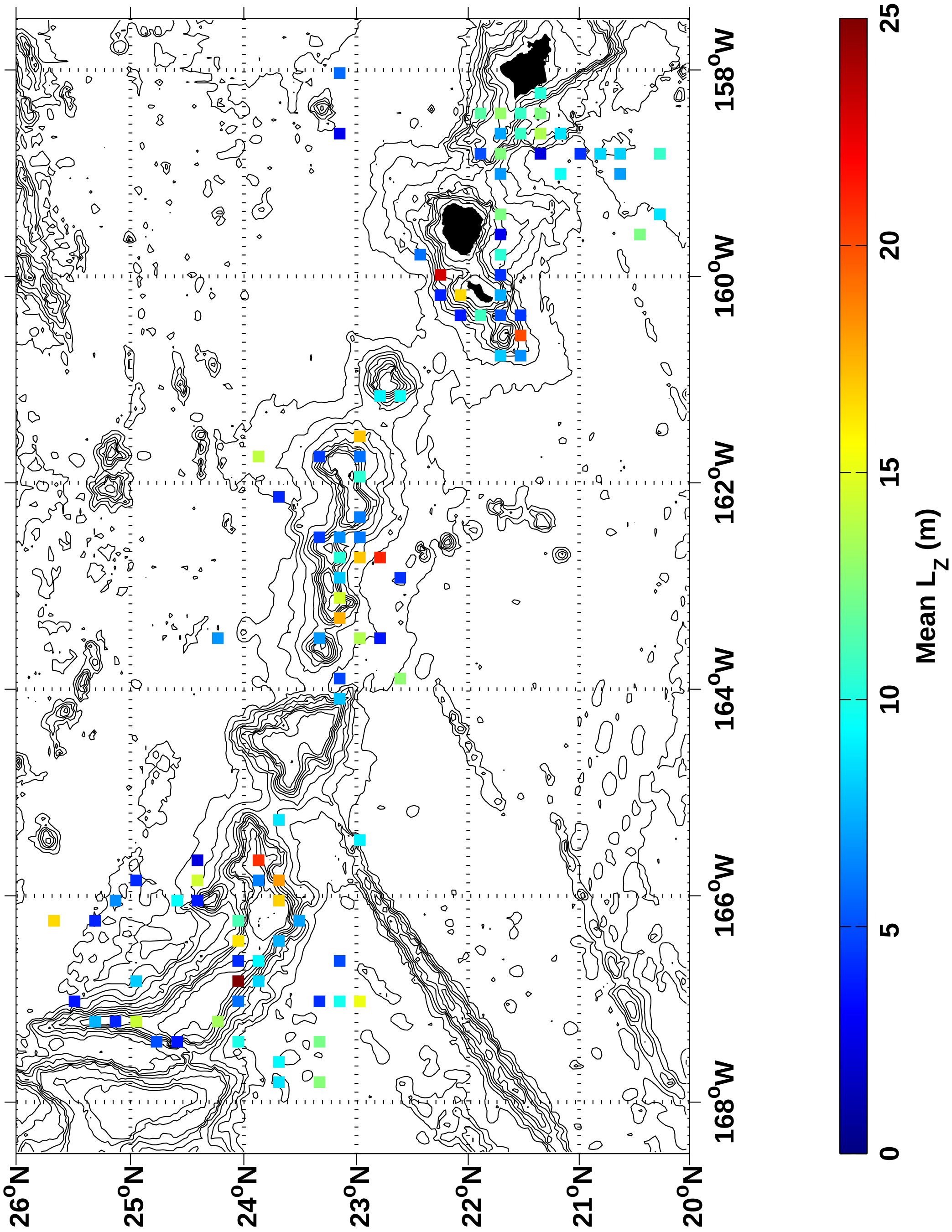

Figure 10: A map of the mean inversion height L_Z where the mean is over all inversions below 100 m depth that fall within the boxes of Fig. 5.

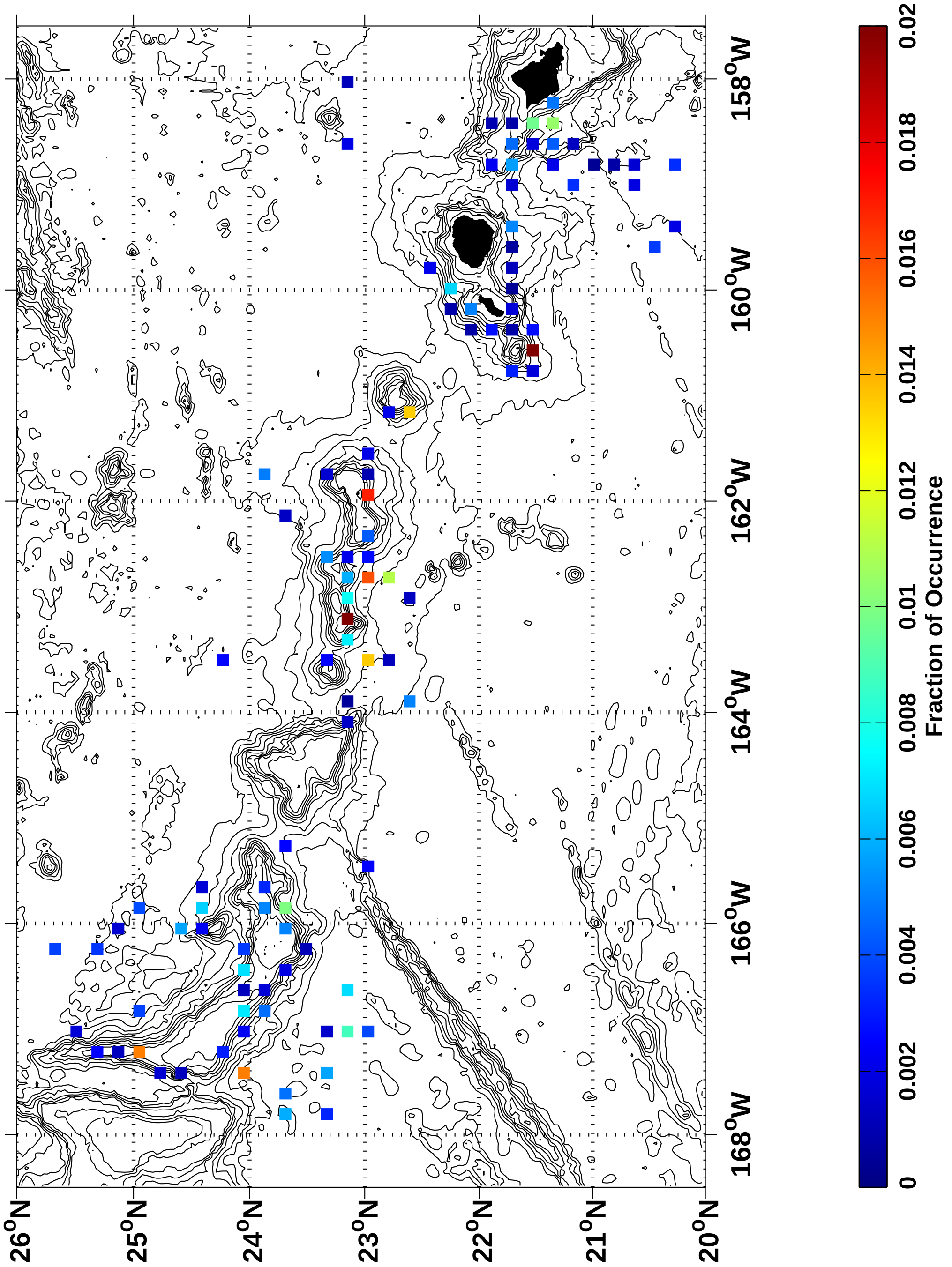

Figure 11: A map of the fraction of occurrence of inversions. The fraction is the sum of L_{Z} over all inversions in each box (boxes defined for Fig. 5) divided by the sum of available depth ranges over all profiles in that box. Simply, it is the mean fraction of the water column that is inverted. The majority of displayed boxes contain one inversion, but one box centered at (23.15°N,163.11°W) contains 14 and several near the ridge in the eastern KC contain more than 5.

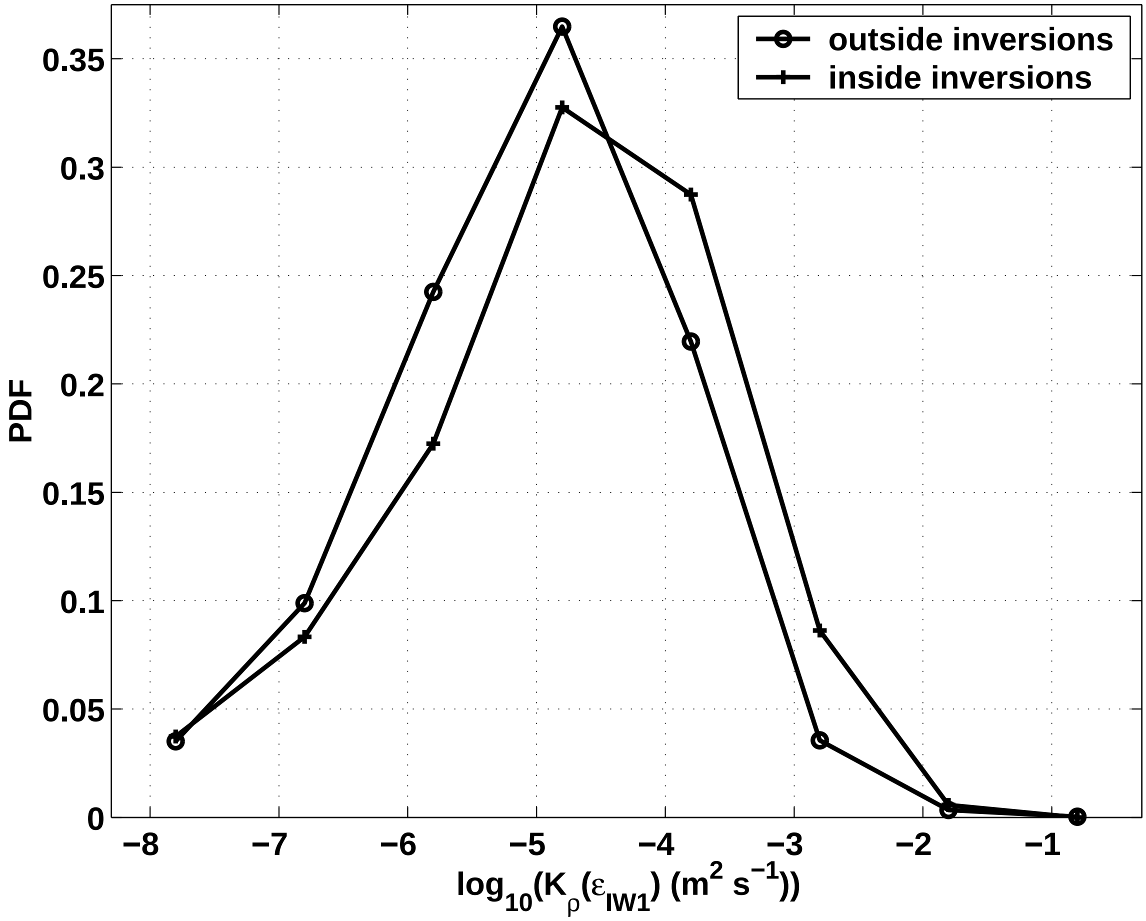

Figure 12: Probability density functions of $\log_{10}(K_\rho(\varepsilon_{\mathrm{IW1}}))$ outside and inside density inversions in the depth range from 100 m to the bottom of the SeaSoar profiles. The range of each bin includes all values that would be considered the same order of magnitude. For example, the range of the fourth bin is 5×10^{-6} to 5×10^{-5} $\mathrm{m}^2\ \mathrm{s}^{-1}$. The first bin, however, contains contributions from a long tail extending several orders of magnitude lower. Values of order 10^{-4} and 10^{-3} $\mathrm{m}^2\ \mathrm{s}^{-1}$ occur more frequently inside inversions than outside inversions.